

1744



3 1176 00102 6583

NACA TN

# NATIONAL ADVISORY COMMITTEE FOR AERONAUTICS

**TECHNICAL NOTE 3363**

LOW-SPEED WIND-TUNNEL INVESTIGATION OF A  
TRIANGULAR SWEEPBACK AIR INLET IN THE

ROOT OF A 45° SWEEPBACK WING

By Arvid L. Keith, Jr., and Jack Schiff

Langley Aeronautical Laboratory  
Langley Field, Va.

**LIBRARY COPY**

FEB 2 1955

LANGLEY AERONAUTICAL LABORATORY  
LIBRARY, NACA  
LANGLEY FIELD, VIRGINIA

**FOR REFERENCE**

**NOT TO BE TAKEN FROM THIS ROOM**



Washington  
January 1955

## NATIONAL ADVISORY COMMITTEE FOR AERONAUTICS

## TECHNICAL NOTE 3363

LOW-SPEED WIND-TUNNEL INVESTIGATION OF A  
TRIANGULAR SWEEPBACK AIR INLET IN THE  
ROOT OF A  $45^\circ$  SWEEPBACK WING<sup>1</sup>

By Arvid L. Keith, Jr., and Jack Schiff

## SUMMARY

A low-speed investigation has been conducted in the Langley two-dimensional low-turbulence tunnel to study a sweptback wing-root air-inlet configuration believed suitable for transonic-speed jet-powered airplanes. The test configurations consisted of a basic model with an NACA 64-008 wing with quarter-chord sweepback of  $45^\circ$  mounted in the mid-wing position on a fuselage of fineness ratio 6.7, and an inlet model which had a triangular-shaped sweptback inlet installed in the wing root. Installation of the wing-root inlet was accomplished with no significant effects on the force characteristics of the basic wing. The fuselage boundary layer entering the inlet was thin and required no boundary-layer-control device ahead of the inlet. Near unity inlet total-pressure recovery was obtained to about 86 percent of the maximum lift coefficient over a large range of inlet-velocity ratio. Maximum local velocities over the external surfaces of the inlet sections were no greater than those over the wing at a midspan station for the assumed high-speed operating conditions.

## INTRODUCTION

Inasmuch as efficient performance of a transonic-speed jet-powered airplane depends importantly on the attainment of high total-pressure recovery in the engine-air-inlet system (reference 1) and on minimum adverse effects of the inlet installation on the external aerodynamic characteristics of the "basic" airplane, careful consideration must be given the inlet design. The difficulties of attaining these design criteria are governed to a large extent by the location of the inlet on the airplane. Considerable design data exist for fuselage-nose and fuselage-side inlets and for inlets in the leading edges of unswept wings (for example, references 2 to 11). However, little information

---

<sup>1</sup>Supersedes the recently declassified NACA RM L50101, "Low-Speed Wind-Tunnel Investigation of a Triangular Sweptback Air Inlet in the Root of a  $45^\circ$  Sweptback Wing" by Arvid L. Keith, Jr., and Jack Schiff, 1950.

is available for design of air inlets located within the wing root, especially for the swept-wing case.

An investigation is being made of a possible swept-wing-root air-inlet configuration for transonic turbojet-powered airplanes. The present preliminary phase of this investigation was conducted at low speed in the Langley two-dimensional low-turbulence tunnel. The basic model, which was used as a reference configuration, consisted of an NACA 64-008 half-span wing with quarter-chord sweepback of  $45^\circ$  in combination with a half-fuselage of fineness ratio 6.7. Installation of a triangular-shaped inlet in the wing root was accomplished by increasing the root chord and thickness. Two modifications were made to the original inlet model in attempts to extend the range of high-inlet-ram recovery to higher lift coefficients. Internal- and external-flow characteristics were evaluated from tuft, total- and static-pressure, and force measurements.

#### SYMBOLS

$C_D$	drag coefficient, $\frac{\text{Drag}}{q_0 S}$
$C_L$	lift coefficient, $\frac{\text{Lift}}{q_0 S}$
$V_i/V_0$	inlet-velocity ratio, $\frac{Q_i}{A_i V_0}$
$A_i$	inlet area
$c$	chord
$H$	total pressure
$\Delta H$	total-pressure loss between free stream and measuring station
$p$	static pressure
$P$	static-pressure coefficient, $\frac{p - p_0}{q_0}$
$Q$	volume rate of flow
$q$	dynamic pressure
$S$	wing area of basic model (4.353 sq ft)
$t$	wing section thickness, expressed in percent $c$

V	velocity
x	distance from leading edge of wing or inlet
$\alpha$	angle of attack of wing-chord line
$\delta$	nominal boundary-layer thickness (defined as normal distance from surface to point where $\frac{H - p_0}{q_0} = 0.95$ )

## General subscripts:

ext	external
int	internal
f	fuselage (used only as $CD_f$ )
i	inlet
o	free stream
T	total

## MODEL CONFIGURATION

The basic model consisted of a semispan wing of  $45^\circ$  quarter-chord sweep mounted with zero incidence in the midwing position on a half-fuselage of fineness ratio 6.7 (figs. 1 and 2(a)). The wing (table I) was composed of NACA 64-008 sections in the streamwise direction and had an aspect ratio of 4.0, a taper ratio of 0.6, no twist, and no dihedral. The fuselage was formed by rotating an NACA 65<sub>2</sub>A015 airfoil section about its chord line.

For the present phase of the investigation a long, thin triangle was selected arbitrarily as the inlet shape in order to avoid abrupt variations in the plan form and in the section thickness ratio of the wing and, at the same time, to minimize the amount of fuselage boundary layer entering the inlet. (See table II and figs. 1 and 2.) A high-speed design inlet-velocity ratio of 0.6 was selected as the minimum value for high-ram pressure recovery, based on previous experience with fuselage-side inlets. The size of the inlet relative to fuselage and wing was

chosen to be representative of a typical single-engine jet airplane assumed to be flying at an altitude of 35,000 feet at a Mach number of 1.0.

In order to permit installation of the inlet, the quarter-chord wing sweep inboard of wing station 13.387 was increased to  $55^\circ$ , the wing chord was increased from the original value at wing station 13.387 to twice the original value at wing station 5.387 (where the leading edge of the basic wing intersected the fuselage), and the wing-section-thickness ratio was increased linearly between these two stations from 8 percent to 13 percent. (See table I.) The leading edge of the new inboard section of the wing was cut off along the line corresponding to the leading edge of the wing outboard of station 13.387, resulting in an increase in thickness ratio at station 5.387 to 16.4 percent. The inlet was then faired in around the selected triangular inlet shape from this new leading edge.

Typical reference lines through the centers of the upper- and lower-inlet-lip radii used in fairing the inlet lips are shown in table II. As indicated by these lines, the triangular inlet was made asymmetrical by locating the center of its base below the chord line in order to provide a thick upper lip such as is desirable from the viewpoint of obtaining a high maximum lift coefficient. Lower-lip stagger, defined as indicated in table II, also was incorporated in each inlet configuration in order to improve the internal-flow characteristics at high angles of attack.

Significant dimensions and features of the three inlet configurations investigated are compared in table II and figure 3. In the case of the original inlet, the triangle formed by the reference lines through the centers of the upper- and lower-lip radii had a width to maximum-height ratio of 3.0; the lower-lip stagger was  $20^\circ$ . Both the external- and internal-lip surfaces incorporated the NACA 1-series non-dimensional ordinates which were developed in reference 2. To form the external shape, these ordinates were applied from the inlet reference line rearward to the maximum-thickness station of the wing section; for the internal shapes, the ordinates were applied from the reference line rearward to a point 0.5 inch back of the inlet lip. The outboard corner of the inlet was faired out by a 0.163-inch radius between the inner surfaces; this corner radius caused a flat in the leading edge of the wing outboard of the inlet which was faired out by a forward protrusion of the wing leading edge (fig. 4).

The inlet as first modified was exactly the same as the original inlet except that the lower lip was cut back to increase the lip stagger to  $30^\circ$ , and thin fairings were added to the inner and outer surfaces of this lip to increase its thickness (table II and fig. 3). On the bottom surface of the wing, the thickening was accomplished by the introduction

of a flat section which extended from the maximum-thickness location to 0.71 inch ahead of maximum thickness at wing station 5.387 and 2.72 inches ahead of the maximum thickness at wing station 11.387. The NACA 1-series ordinates were then applied from the lip reference line to the start of this flat section rather than to the maximum-thickness station.

In the final inlet, the lip stagger was further increased in the outboard part of the inlet, the upper-lip reference line was drooped, and the inner-lip fairings of both the upper and lower lips were thickened (table II and fig. 3). At the same time greater lip thicknesses in the vicinity of the nose were obtained by the substitution of elliptical ordinates for the NACA 1-series ordinates used previously. The drooped top lip and the thicker inner-lip fairings reduced the minimum inlet-flow area approximately 12 percent. As shown in figure 4, the increase in lip stagger in the outboard part of the inlet eliminated the necessity for the protruded nose fairing used in the previous configurations.

Dimensions of the external- and internal-lip shapes of the final configuration are presented in table III. Dimensions of the internal fairing of the upper surface of the duct necessitated by drooping the upper lip of the final configuration are given in table IV, and dimensions of wing-inlet junction station 13 are given in table V.

#### METHODS AND TESTS

Each of the several test configurations was mounted on a three-component tunnel balance system with the support point at fuselage station 29 (fig. 1). A  $\frac{1}{2}$ - by 4-inch duralumin bar 40 inches long attached the wing tip to the balance. The clearance between the model and each tunnel wall was  $\frac{1}{4}$  inch. Internal flow was induced and controlled by a variable-speed centrifugal blower and the flow quantity was measured by a calibrated orifice meter. The internal flow was discharged from the model in a direction normal to the tunnel walls and was then ducted through a frictionless seal to the blower.

Inlet total-pressure recoveries were determined from measurements of shielded total-pressure tubes distributed spanwise along the inlet center line and in vertical planes at semispan stations 6.5 and 10. The shielded tubes had a 0.050-inch-outside-diameter total-pressure tube located directly in the center of a 1/8-inch-outside-diameter shield that was flared at the forward end. The rearward distance of these tube rakes from the lower lip varied linearly from  $3\frac{3}{4}$  inches at the most inboard measuring station to 1 inch at the outboard station. Surface-pressure

measurements at wing stations 6.5 and 10 were obtained on the upper and lower lips by flush orifices which extended from well inside the lip to about 60 percent of the chord on the external surface. Other rows of surface-pressure orifices were provided at station 13, the transition section between the ducted root section and the basic wing, and on the fuselage side near the wing-fuselage juncture. Fuselage orifices were also provided on the basic model.

Boundary-layer surveys were made along the fuselage surface and just inside the inlet using a rake of 0.040-inch-outside-diameter total- and static-pressure tubes. The total tubes in this rake were flattened on the ends to a 0.004-inch opening. These surveys were made with the fuselage nose aerodynamically smooth and with transition fixed at the nose by a 3-inch-wide band of roughness (0.008- to 0.012-inch-diameter carborundum grains).

Flow directions on the fuselage, in and around the inlet, and on the wing were observed by a tuft on a wand. All model pressure measurements were recorded by photographing a multitube manometer. The differential orifice meter pressures were read visually from a multitube manometer.

Although the force data are not correct quantitatively because of the type of model mount and the unknown tunnel-wall effects for this type of mount, the effects of addition of the wing-root inlet on the lift and external-drag characteristics can be determined by comparison of the inlet model and the basic model. In order to obtain comparative external drags, however, the drag equivalent of the internal flow of the inlet model must be removed from the measured drags. This operation was accomplished by use of the relations

$$C_{D_{\text{ext}}} = C_{D_T} - C_{D_{\text{int}}} + C_{D_F}$$

and

$$C_{D_{\text{int}}} = 2 \left( \frac{A_1}{S} \right) \left( \frac{V_1}{V_0} \right)$$

where  $2(A_1/S)(V_1/V_0)$ , valid for incompressible flow, is the drag equivalent of the loss in momentum of the internal flow caused by bringing the internal flow to rest in the stream direction before discharging it from the model (fig. 1). The term  $C_{D_F}$  is the drag coefficient corresponding to the total-pressure losses of the entering flow as determined from boundary-layer measurements just inside the entrance.

Pressure surveys and force measurements of each configuration were conducted for a range of inlet-velocity ratios, 0 to 1.5, and for a

range of angles of attack,  $-10^{\circ}$  to  $30^{\circ}$ . All tests were conducted at a tunnel airspeed of 100 miles per hour which corresponds to a Mach number of 0.13 and a Reynolds number of  $1.4 \times 10^6$  based on the wing mean aerodynamic chord.

## RESULTS AND DISCUSSION

Results obtained with the original and modified inlets are first discussed briefly to indicate the considerations which motivated the inlet modifications and to show the extent to which these modifications affected the aerodynamic characteristics of the model. The final inlet model is then discussed in detail and compared with the basic unducted model.

### Original and Modified Inlets

Total-pressure distributions at the center line and two vertical measuring stations of the original inlet are presented in figure 5; points where double symbols are used show that the total-pressure coefficient is constant between these two values of inlet-velocity ratio. At  $\alpha = 0^{\circ}$  (figs. 5(a), 5(b), and 5(c)), a total-pressure coefficient of nearly unity was obtained for the greater part of the inlet for inlet-velocity ratios of 0.59 and above. Tuft studies of the flow in and around the inlet showed that the large apparent losses in total pressure in the outboard section at inlet-velocity ratios less than 0.59 (fig. 5(a)) were caused by misalignment of the measuring tubes with the flow due to spanwise outflow from this region. Localized losses in the outboard corner at the highest flow rate and in the inboard corner for all flow rates were caused by separation from the outboard-corner radius and intake of the fuselage boundary layer, respectively. A detailed discussion of the fuselage boundary layer will be presented later in the section entitled "Final Inlet."

Small increases in angle of attack caused insignificant changes in the inlet total-pressure distributions. As the angle was increased to  $6^{\circ}$ , however, formation of bubbles of separation at the inner surface of the lower lip in the outboard section of the inlet occurred at a  $V_1/V_0$  just greater than 1.0, as indicated from tufts and from measurements obtained by a reference total-pressure tube near the surface. With further increases in angle of attack to  $10^{\circ}$ , the flow in the outer third of the inlet was completely separated for most of the inlet-flow conditions; this separation caused large losses in total pressure (figs. 5(d) and 5(f)).



Incorporation of additional stagger and inner-lip thickness of the lower lip in the case of the modified inlet (table II) reduced the angularity of flow and total-pressure losses in the outboard section considerably at  $\alpha = 0^\circ$  (fig. 5(a)) and reduced the extent of the separated region for the high angle-of-attack condition (figs. 5(d) and 5(f)). However, the total-pressure recovery still was unsatisfactory. For the final configuration, therefore, the lower-lip stagger and inner-lip thickness were further increased in the outboard region of the inlet, table II.

Surface pressure distributions measured on the external lips of the original inlet (fig. 6) and the modified inlet were similar in nature to those measured on the NACA 1-series cowlings of references 2 to 6; the curves for several test inlet-velocity ratios have been omitted for clarity in the figure. The ranges of inlet-velocity ratio and angle of attack for peak-free operation on these inlet lips, however, were much smaller than desired for an inlet of this type (fig. 7). Because of this consideration the upper lip of the final inlet was drooped in the outboard section of the inlet, and the internal and external lips were made blunter by replacing the NACA 1-series ordinates with elliptical ordinates (tables II and III).

#### Final Inlet

Aerodynamic forces.- Comparisons between the lift and external-drag characteristics of the basic-wing model and the final inlet model are presented in figures 8 and 9 for several inlet-velocity ratios. Installation of the ducted-root section did not cause any significant changes in the angle of zero lift or the lift-curve slope (fig. 8(a)) even for the zero-inlet-velocity-ratio case. Because of the thickened root, however, the minimum drag at low inlet-velocity ratios was somewhat higher than for the basic wing (figs. 8(b) and 9). Increases in the inlet-velocity ratio effected reductions in drag such that at a value of 0.8 and above minimum external-drag coefficients comparable to the basic wing were obtained.

In the region of near maximum lift of the wing, lift coefficients for the inlet model were slightly higher than those for the basic model, probably in part due to the additional lift of the fillet. Inasmuch as the lift coefficients of the inlet model in this region decrease regularly with increases in inlet-velocity ratio, it appears that a part of the increase in lift may also have been caused by a vortex type of flow (such as described in reference 12) originating from the outboard corner of the inlet; the strength of these vortices would be expected to decrease with increases in inlet-velocity ratio. The effect of increases in the inlet-velocity ratio on the external-drag coefficients for this range of lift coefficient was much more pronounced than for the

low-lift-coefficient range (fig. 9). The favorable effect of increases in inlet-velocity ratio on the drag coefficients at high lift is probably due to a decrease in the boundary-layer growth and flow separation because of the decrease in the adverse pressure gradient near the leading edge of the wing.

Flow over fuselage nose.- Static-pressure distributions over the fuselage nose in the plane of the wing chord are presented in figure 10. At an angle of attack of  $0^\circ$ , the maximum local velocity remained sub-stream up to an inlet-velocity ratio of about 0.6. Thus, as in the case of the transonic inlets discussed in references 5 and 6, adverse-shock-boundary-layer interaction effects on the entering flow will probably be avoided up to some small supersonic Mach number; an inlet total-pressure recovery of 0.96 ( $H_0 - p_0$ ) was obtained at the highest test Mach number of 1.19 for the fuselage-side inlet discussed in reference 6. With an increase in angle of attack to  $10^\circ$ , negative pressure coefficients occurred ahead of the inlet; this condition, however, represents a much lower flight speed attitude, so that no large adverse compressibility effects would be expected.

The large pressure rise in the immediate vicinity of the inlet, at the lower inlet-velocity ratios, had important effects on the fuselage boundary layer. Total-pressure distributions within natural and artificially thickened fuselage boundary layers are presented in figure 11 for a position just inside the inlet. Nearly linear increases in boundary-layer thickness occurred with decreases in the inlet-velocity ratio from 1.5 to 0.40; with further decreases, the thickness increased more rapidly and the boundary layer soon separated. Upon fixing transition at the fuselage nose, considerable increases in thickness occurred at the lower flow rates; the inlet-velocity ratio required to avoid separation, however, was increased only slightly. An increase in angle of attack to  $10^\circ$  caused some distortion in the boundary sublayer for both the natural- and fixed-transition cases, due probably to crosswise flow within the layer. The total thickness, however, was not materially affected by increases in angle of attack, nor was the separation-free inlet-velocity ratio increased significantly. Thus, boundary-layer control ahead of the entrance does not appear to be required for this type of inlet at speeds below which shock-boundary-layer interaction effects may become important.

Growth of the fuselage boundary layer is summarized in figure 12. The effect of fixing transition at the nose was to increase the boundary-layer thickness everywhere rearward of this point. The fact that the curves for the two boundary layers are essentially parallel downstream of station 19 for each of the three inlet-velocity ratios shown again indicates that the minimum inlet-velocity ratio necessary to avoid separated flow entering the inlet is relatively insensitive to the point at which transition occurs ahead of the inlet.

Flow in inlet.- Static-pressure distributions around the nose sections of the inlet are presented in figure 13. With increases in inlet-velocity ratio, the effective angles of attack of the inner surfaces of the inlet lips increased, as shown by the outward displacement of the positive-pressure region at the nose, and large negative-pressure peaks occurred on these surfaces. Inasmuch as the outboard inner-lip fairings were relatively thin, the effect of increasing inlet-velocity ratio on the maximum velocities over these surfaces, indicated by the minimum surface pressure coefficients (fig. 14), was much more pronounced than for the inboard sections.

Total-pressure distributions at the center line and the two vertical stations of the inlet are presented in figure 15 for lift coefficients ranging from -0.39 to 1.01 and inlet-velocity ratios ranging from 0 to 1.5; points where double symbols are used show that the total-pressure coefficient is constant between these two values of inlet-velocity ratio. At  $\alpha = -5^\circ$  ( $C_L \approx -0.39$ ) the flow separated from the inner surface of the upper lip in the outboard section of the inlet in the higher range of inlet-velocity ratio and caused large losses in inlet total pressure (fig. 15(a)). When the angle of attack was increased to  $-3^\circ$  ( $C_L \approx -0.22$ ), however, visual tuft and manometer observations showed that separation from the upper lip did not occur at inlet-velocity ratios greater than 0.40, and a total-pressure coefficient of nearly unity was obtained over most of the inlet. The total-pressure recovery in the outboard corner of the inlet was reduced substantially at inlet-velocity ratios below 0.40 by a spanwise outflow along the face of the inlet. The flow phenomena and pressure recovery at an angle of attack of  $0^\circ$  ( $C_L \approx 0.06$ ) (fig. 15(b)) were essentially the same as that for  $\alpha = -3^\circ$ .

Small increases in angle of attack above  $0^\circ$  caused no significant effects on the inlet total-pressure recovery (fig. 15(c)). With further increases in angle to  $10^\circ$  ( $C_L \approx 0.83$ ) small localized losses began to occur near the lower inner-lip surfaces (fig. 15(d)). At  $\alpha = 12^\circ$  ( $C_L \approx 0.92$ ), these losses in the outboard part of the inlet increased rapidly at any inlet-velocity ratio greater than 1.2 (fig. 15(e)), indicating the formation of bubbles of separation. These losses again were localized and did not cause appreciable changes in the distributions. At an angle of attack of  $15^\circ$  ( $C_L \approx 1.01$ ), extensive separation occurred from the inner surface of the lower lip in the outboard section of the inlet (fig. 15(f)) and caused important losses in inlet total-pressure recovery at this point. The separation bubble had also progressed toward the inboard section, but here the losses were confined to a region very near the surface.

Average inlet total-pressure coefficients could not be determined accurately for the various test conditions because of the necessarily limited pressure-tube instrumentation in the outboard portion of the

inlet. Inasmuch as this parameter is important in determining the inlet performance, average inlet total-pressure recoveries were determined by extrapolating the data obtained to this portion of the inlet. The ranges of inlet-velocity ratio and lift coefficient for which the inlet total-pressure recovery was  $0.90q_0$  or greater are presented in figure 16. For the range of inlet-velocity ratio from 0.4 to the maximum test value of 1.5, low inlet losses were maintained to approximately 86 percent of the maximum  $C_L$ . (See fig. 8.) The assumed high-speed design inlet-velocity ratio of 0.6 for the present configuration is shown to be conservative; in the low-lift-coefficient range, inlet-velocity ratios as low as 0.3 could have been selected without incurring important inlet total-pressure losses. Lower values of  $V_i/V_0$  for the high-speed attitude would decrease the internal ducting losses and would result in correspondingly lower inlet-velocity ratios throughout the speed range. It is noted that the effect of inlet-velocity ratio on the external drag must also be considered in selecting a lower design inlet-velocity ratio. (See fig. 9.)

Flow over external surfaces.- Static-pressure distributions over the inlet-lip sections and the inlet-wing transition section are presented in figure 17; the curves of several test inlet-velocity ratios have been omitted for clarity in the figure. Excepting the upper surface of station 6.5, the thickest section, each of the several stations had sharp negative-pressure peaks on the nose at low inlet-velocity ratios. With sufficient increases in  $V_i/V_0$  to remove these localized pressure peaks, essentially uniform pressure distributions were obtained at the lower angles of attack. Inasmuch as the lower-lip sections were somewhat thinner than the upper sections, greater values of  $V_i/V_0$  were required to obtain uniform distributions over these surfaces. Increases in the angle of attack from  $0^\circ$  to  $4^\circ$  ( $C_L \approx 0.40$ ) caused much sharper nose peaks over the upper sections and required greater values of  $V_i/V_0$  to remove these peaks; the maximum test  $V_i/V_0$  was not sufficient to remove the nose peaks at the transition section at this angle-of-attack condition. With further increases in angle of attack to  $6^\circ$  ( $C_L \approx 0.58$ ), the maximum test  $V_i/V_0$  was not sufficient to remove the nose peaks for any of the upper-surface sections. Distributions over the upper surface of the wing at the midspan station (fig. 18) showed similar angle-of-attack effects. At  $\alpha = 0^\circ$ , the distribution was essentially uniform up to the maximum-thickness station. Increases in angle of attack produced sharp negative nose pressure peaks which increased in magnitude with further increases in angle.

Minimum surface pressure coefficients for the several measuring stations over the inlet, indicative of the maximum local velocities over the external surfaces, are presented in figure 19 as a function of inlet-velocity ratio. Included also, for comparison, are the minimum pressures over the upper surface of the wing at the midspan station; these pressures are denoted by points at zero-inlet-velocity ratio. Above an

inlet-velocity ratio of 0.80 the minimum pressures over the root inlet and the inlet-wing transition section were no greater than those for the midspan wing station over the lift-coefficient range of 0 to approximately 0.40. An approximate method for converting low-speed values to equivalent values of the high-speed inlet-velocity ratio, presented in reference 3, indicates that peak-free operation will be obtained to an inlet-velocity ratio of 0.60 at a Mach number of 1.0, the values selected for high-speed operation in the present case. Experimental data obtained recently (references 4 to 6) indicate that peak-free operation may be maintained to even lower values of inlet-velocity ratio. Exact evaluation of the effect of installation of the wing-root inlet on the external-drag characteristics of the wing, however, can be determined only by tests at high speeds.

Wing-fuselage juncture effects. - Pressure distributions along the fuselage in planes equidistant above the upper surface of the wing of the basic model and of the inlet model are presented in figure 20. The pressure distributions and values of the minimum pressures for each configuration were approximately the same. It is believed, therefore, that installation of the present wing-root inlet should cause no severe adverse interference effects at high speed.

#### SUMMARY OF RESULTS

A low-speed investigation has been conducted in the Langley two-dimensional low-turbulence tunnel to study a sweptback wing-root air-inlet configuration believed suitable for transonic jet-powered airplanes. The more important conclusions of the investigation of the basic model and the final inlet model are summarized as follows:

1. Installation of the ducted-root section had no significant effects on the external drag, angle of zero lift, lift-curve slope, or maximum lift of the basic model.

2. The fuselage boundary layer entering the inlet remained thin and did not separate even for inlet-velocity ratios considerably below the assumed high-speed design value; therefore, no boundary-layer-control device was required ahead of the inlet.

3. Near unity inlet total-pressure recovery was obtained to about 86 percent of the maximum lift coefficient for a large range of inlet-velocity ratio.

4. Minimum pressures over the external surfaces of the inlet, indicative of the local maximum velocities, were no greater than those at the midspan wing station for the assumed high-speed operating conditions.

Langley Aeronautical Laboratory,  
National Advisory Committee for Aeronautics,  
Langley Field, Va., August 25, 1950.

## REFERENCES

1. Hanson, Frederick H., Jr., and Mossman, Emmet A.: Effect of Pressure Recovery on the Performance of a Jet-Propelled Airplane. NACA TN 1695, 1948.
2. Baals, Donald D., Smith, Norman F., and Wright, John B.: The Development and Application of High-Critical-Speed Nose Inlets. NACA Rep. 920, 1948.
3. Nichols, Mark R., and Keith, Arvid L., Jr.: Investigation of a Systematic Group of NACA 1-Series Cowlings with and without Spinners. NACA Rep. 950, 1949.
4. Pendley, Robert E., and Smith, Norman F.: An Investigation of the Characteristics of Three NACA 1-Series Nose Inlets at Subcritical and Supercritical Mach Numbers. NACA RM L8L06, 1949.
5. Pendley, Robert E., and Robinson, Harold L.: An Investigation of Several NACA 1-Series Nose Inlets with and without Protruding Central Bodies at High-Subsonic Mach Numbers and at a Mach Number of 1.2. NACA RM L9L23a, 1950.
6. Pendley, Robert E., Robinson, Harold L., and Williams, Claude V.: An Investigation of Three Transonic Fuselage Air Inlets at Mach Numbers from 0.40 to 0.94 and at a Mach Number of 1.19. NACA RM L50H24, 1950.
7. Frick, Charles W., Davis, Wallace F., Randall, Lauros M., and Mossman, Emmet A.: An Experimental Investigation of NACA Submerged-Duct Entrances. NACA ACR 5120, 1945.
8. Hall, Charles F., and Barclay, F. Dorn: An Experimental Investigation of NACA Submerged Inlets at High Subsonic Speeds. I - Inlets Forward of the Wing Leading Edge. NACA RM A8B16, 1948.
9. Racisz, Stanley F.: Development of Wing Inlets. NACA ACR L6B18, 1946.
10. Bartlett, Walter A., Jr., and Goral, Edwin B.: Wind-Tunnel Investigation of Wing Inlets for a Four-Engine Airplane. NACA RM L6L11, 1947.
11. Dannenberg, Robert E.: A Design Study of Leading-Edge Inlets for Unswept Wings. NACA RM A9K02b, 1950.

12. Lange, Roy H., Whittle, Edward F., Jr., and Fink, Marvin P.:  
Investigation at Large Scale of the Pressure Distribution and  
Flow Phenomena over a Wing with the Leading Edge Swept Back  $47.5^\circ$   
Having Circular-Arc Airfoil Sections and Equipped with Drooped-  
Nose and Plain Flaps. NACA RM L9G15, 1949.



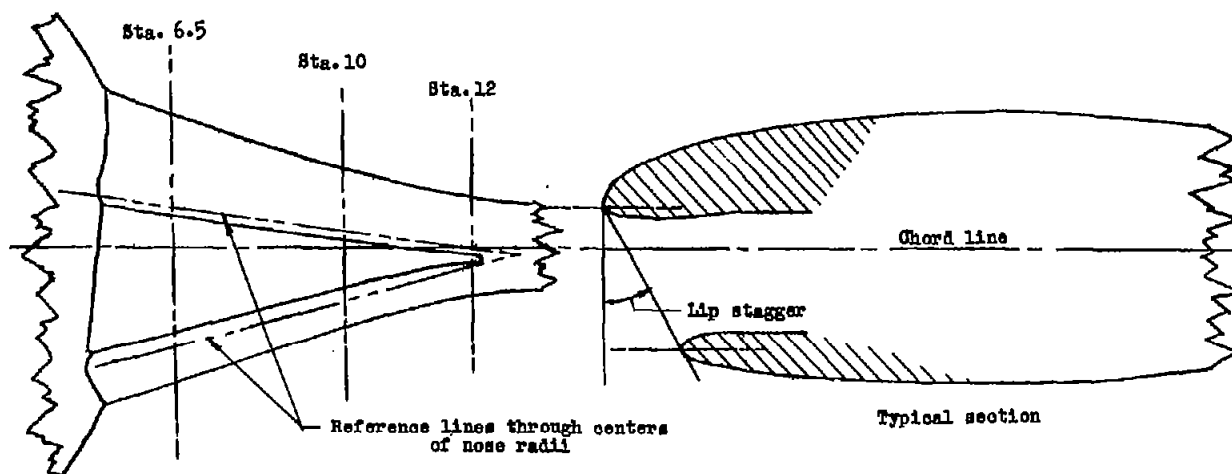
TABLE I - DIMENSIONS OF BASIC AND DUCTED WINGS

Wing station	Basic wing			Ducted wing			
	c (in.)	t (percent c)	c/4 sweep	Total c (in.) (a)	t (percent c)	c/4 sweep	Inlet c (in.) (b)
0	22.347	8	45°				
<sup>c</sup> 5.387	21.000	8	45°	42.000	13	55°	33.325
6.500	20.722	8	45°	38.160	12.3	55°	30.849
8.250	20.285	8	45°	32.076	11.2	55°	26.928
10.000	19.847	8	45°	26.060	10.04	55°	23.062
12.000	19.347	8	45°	20.434	8.80	55°	19.572
<sup>d</sup> 12.358	19.258	8	45°	19.938	8.55	55°	19.320
13.000	19.097	8	45°	19.323	8.10	55°	19.102
13.137	19.063	8	45°	19.205	8	55°	19.063
13.387	19.000	8	45°	19.000	8	45°	19.000
18.000	17.847	8	45°	17.847	8	45°	17.847
36.000	13.347	8	45°	13.347	8	45°	13.347

- (a) Chord before installation of inlet.  
 (b) Leading edge of ducted wing coincident with leading edge of basic wing.  
 (c) Juncture of fuselage with leading edge at fuselage station 20.00.  
 (d) Outboard corner of inlet.



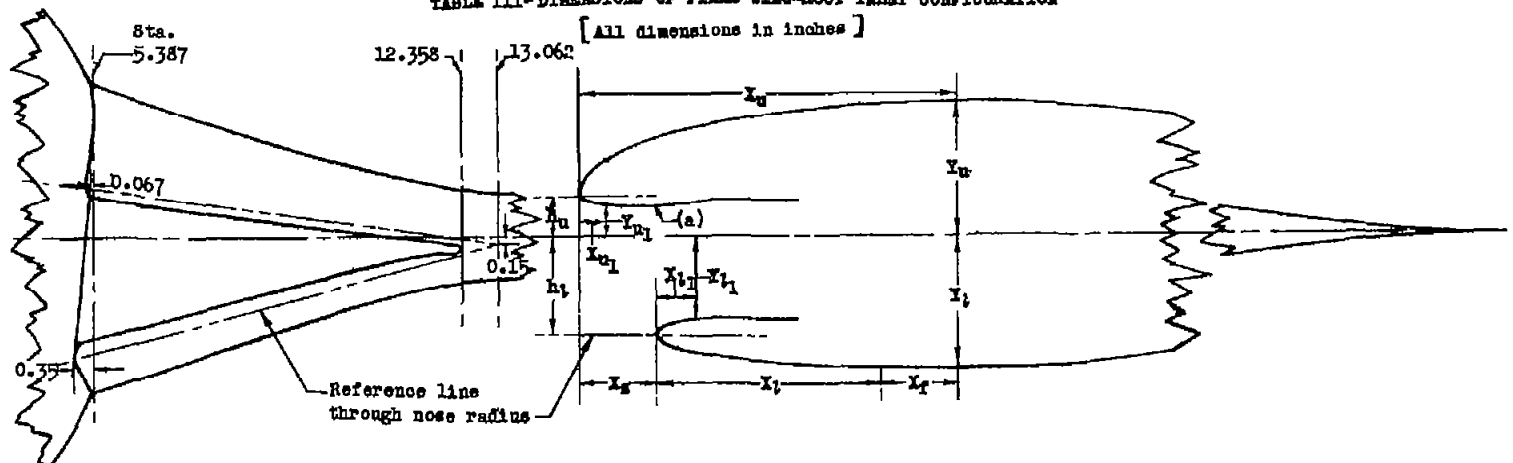
TABLE II - COMPARISON OF THE SEVERAL INLET CONFIGURATIONS



Station	Inlets								
	Original			Modified			Final		
	6.5	10	12	6.5	10	12	6.5	10	12
Dimensional quantities									
Lip stagger, degrees	20	20	20	30	30	30	30	41.23	62.26
Distance from upper reference line to chord line, inches	.709	.365	1.67	.709	.365	.167	.709	.251	-.011
Distance from lower reference line to chord line, inches	1.732	.888	.406	1.732	.888	.406	1.732	.888	.406
Upper inner lip thickness measured from reference line, inches	.096	.055	.035	.096	.055	.035	.150	.150	.100
Lower inner lip thickness measured from reference line, inches	.192	.110	.070	.240	.155	.105	.300	.260	.177
Lip ordinates, non-dimensional	NACA 1-series						Elliptical		
Minimum inlet area, sq in.	10.74			10.29			9.40		

NACA

TABLE III-DIMENSIONS OF FINAL WING-ROOT INLET CONFIGURATION



Wing station	External surfaces (b)								Internal surfaces (b)			
	$h_u$	$X_u$	$Y_u$	$X_g$	$h_l$	$X_l$	$X_l^{(c)}$	$Y_l$	$X_{u1}$	$Y_{u1}$	$X_{l1}$	$Y_{l1}$
5.387	0.854	7.285	2.730	1.542	2.000	5.743	0	2.730	0.500	0.704	0.750	1.687
6.500	.709	7.190	2.347	1.409	1.732	5.781	0	2.347	.500	.559	.750	1.432
8.250	.480	7.041	1.803	1.200	1.310	4.966	1.875	1.803	.500	.330	.750	1.030
10.000	.251	6.905	1.308	.991	.888	4.164	1.750	1.308	.500	.101	.750	.628
12.000	-.011	6.910	.899	.751	.406	3.409	2.750	.899	.250	-.111	.750	.229

NACA

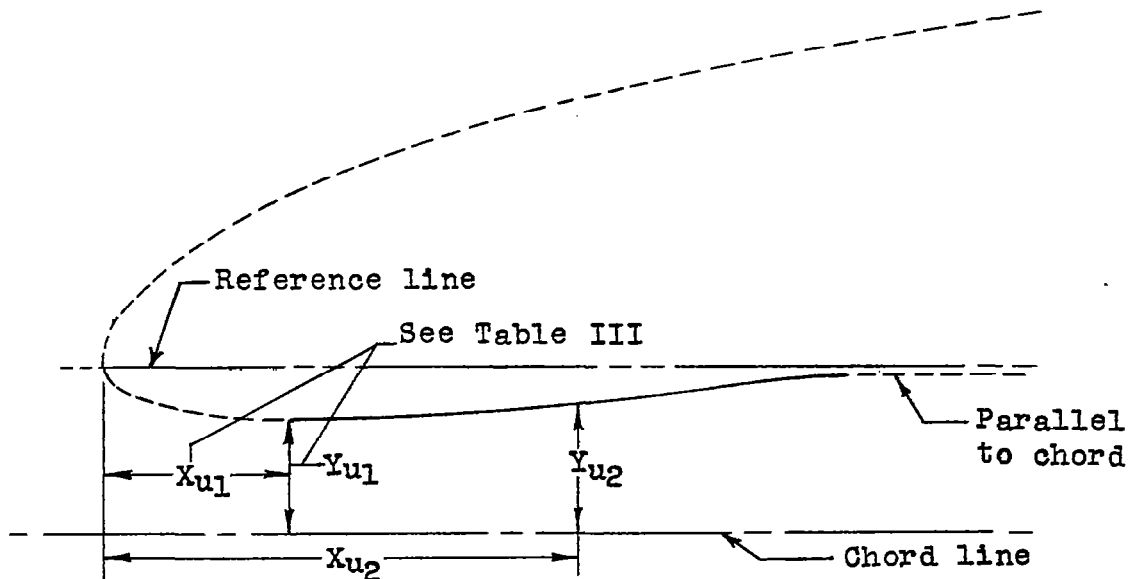
(a) Rearward section of upper inner lip faired from  $X_{u1}$ . (See Table IV.)

(b) External and internal nose shapes determined from elliptical ordinates.

(c) Flat on lower surface.

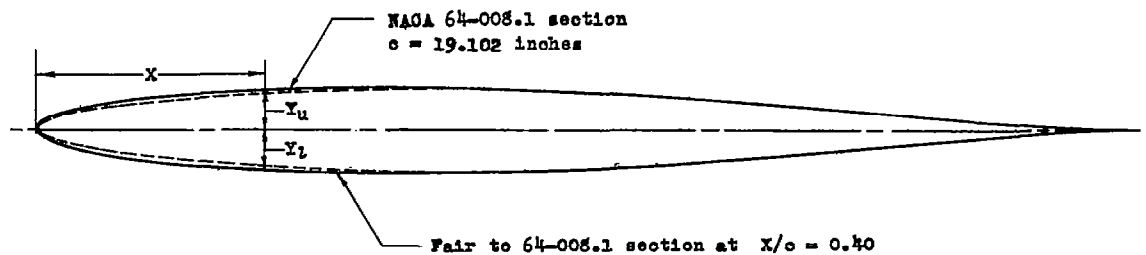
TABLE IV— ORDINATES FOR FAIRED UPPER INNER LIP SURFACE  
OF FINAL INLET CONFIGURATION

[ All dimensions in inches ]



Station 6.5		Station 8.25		Station 10		Station 12	
$X_{u2}$	$Y_{u2}$	$X_{u2}$	$Y_{u2}$	$X_{u2}$	$Y_{u2}$	$X_{u2}$	$Y_{u2}$
0		0		0		0	
.500	0.559	.500	0.330	.500	0.101	.250	-0.110
.700	.559	.700	.330	.700	.112	.300	-.109
.900	.561	.900	.340	.900	.138	.500	-.092
1.100	.566	1.100	.356	1.100	.178	.700	-.066
1.300	.570	1.300	.375	1.300	.222	.900	-.025
1.500	.578	1.500	.401	1.500	.270	1.000	-.001
1.700	.587	1.700	.430	1.600	.284	1.100	.025
1.900	.596	1.900	.455	1.700	.308	1.300	.075
2.100	.605	2.000	.462	1.750	.310	1.500	.110
2.300	.611					1.700	.130
2.500	.613					1.900	.144
						2.000	.145

TABLE V - ORDINATES OF WING-INLET JUNCTURE (STATION 13) FOR FINAL INLET CONFIGURATION



X	$Y_u$	$Y_l$
0	0	0
.13	.41	.31
.26	.58	.46
.52	.80	.68
1.04	1.11	.99
1.55	1.32	1.22
2.59	1.68	1.63
3.89	2.04	2.05
7.50	2.71	2.73
10.00	3.05	3.05
15.00	3.52	3.52
20.00	3.86	3.86
25.00	4.06	4.06
30.00	4.17	4.17
35.00	4.15	4.15
40.00	4.04	4.04

All values given in percent of  
 airfoil chord



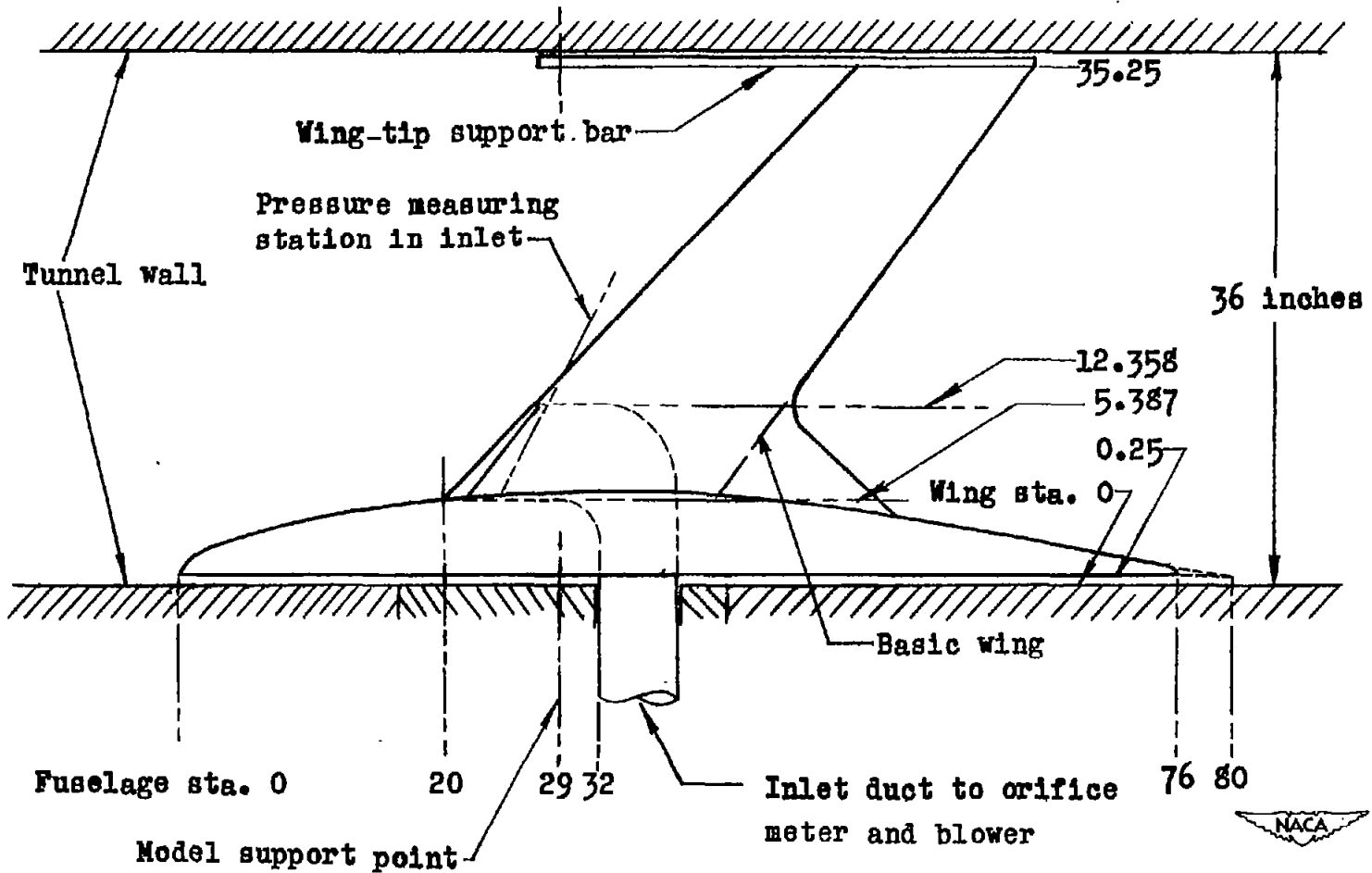
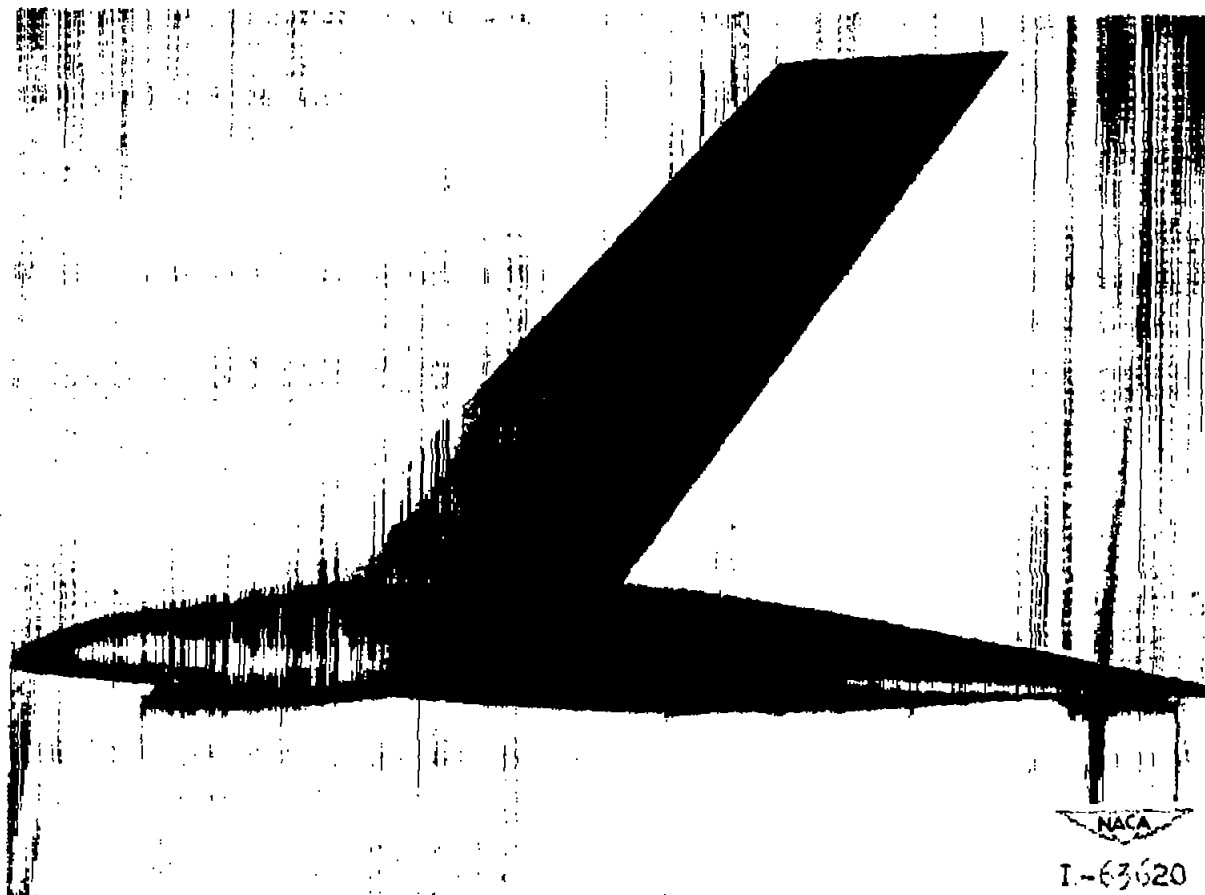
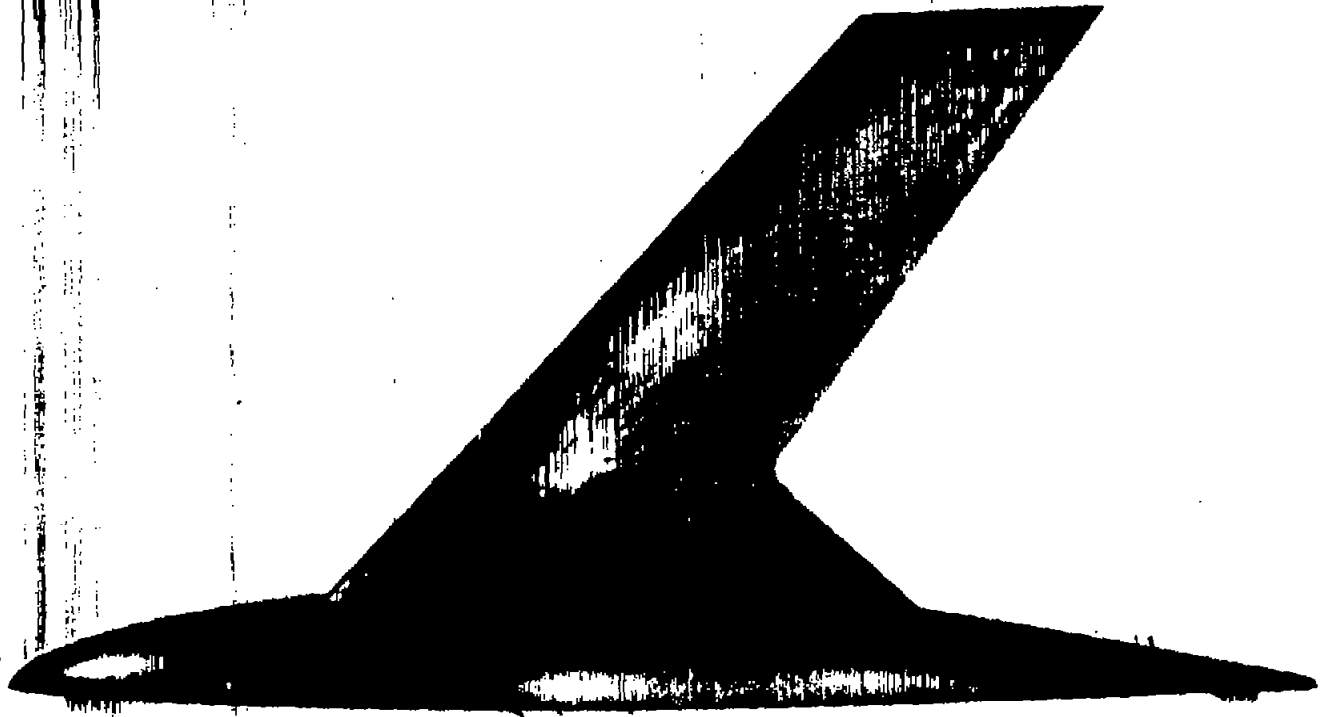


Figure 1.- General arrangement of inlet model in tunnel, bottom view.



(a) Basic wing model, plan view.

Figure 2.- Views of models.

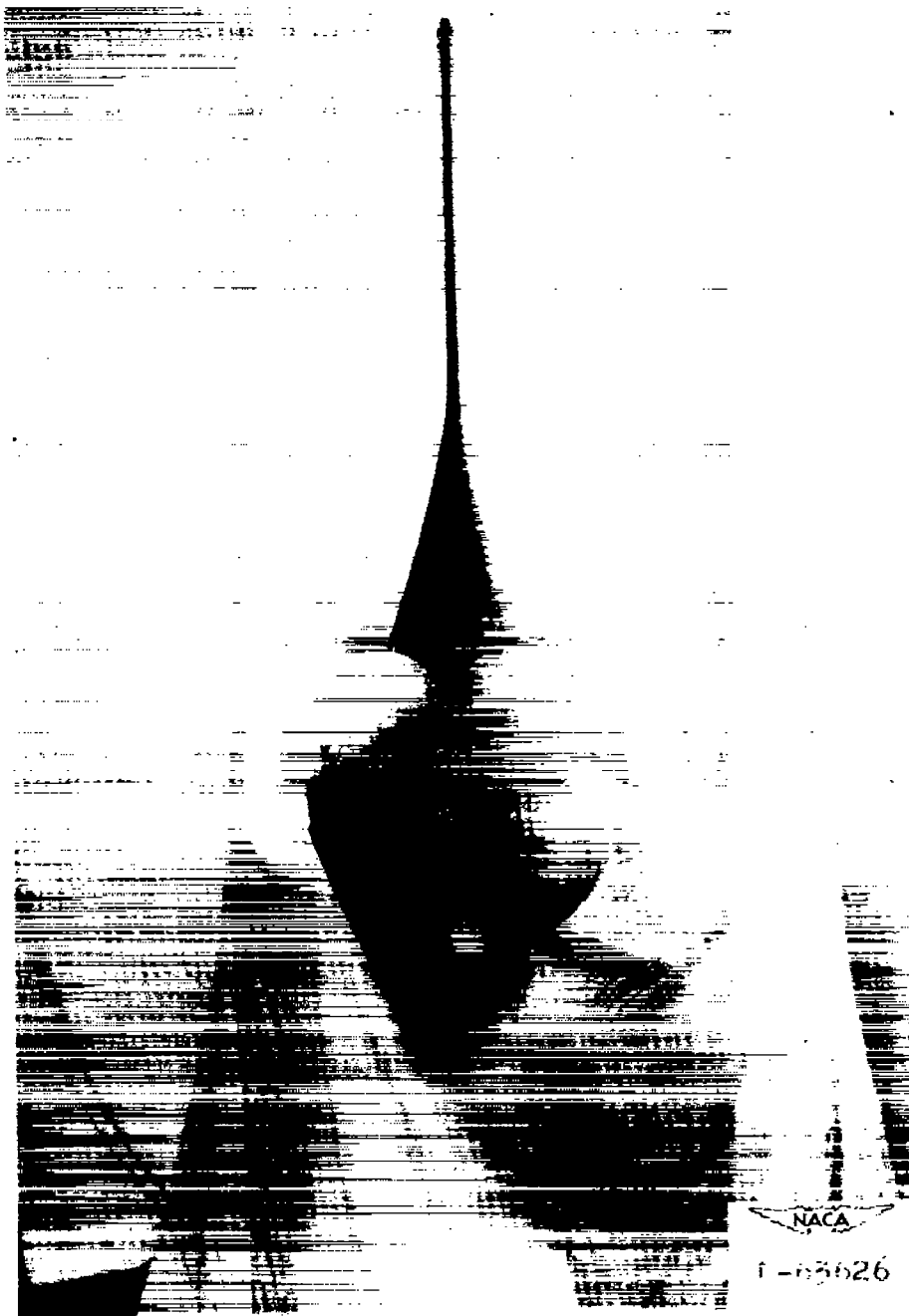


NACA  
L-63624

(b) Final inlet model, plan view.

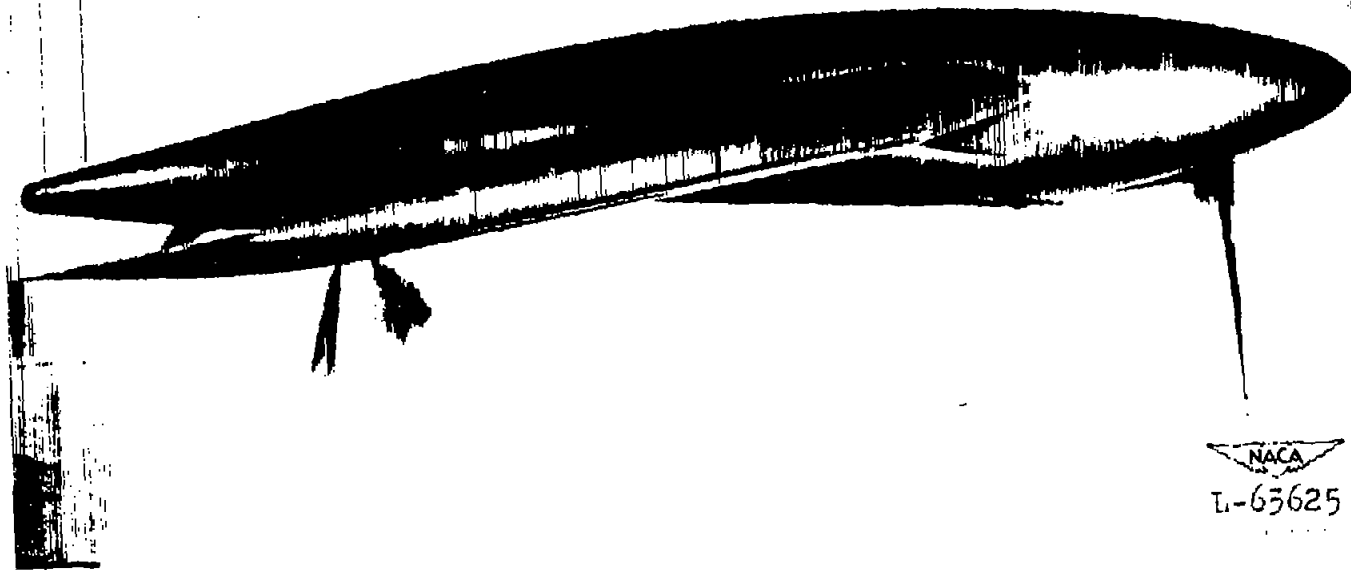
Figure 2.- Continued.





(c) Final inlet model, front view.

Figure 2.- Continued.



(d) Final inlet model, side view.

Figure 2.- Continued.



(e) Final inlet model, 3/4 front view from lower side.

Figure 2.- Concluded.

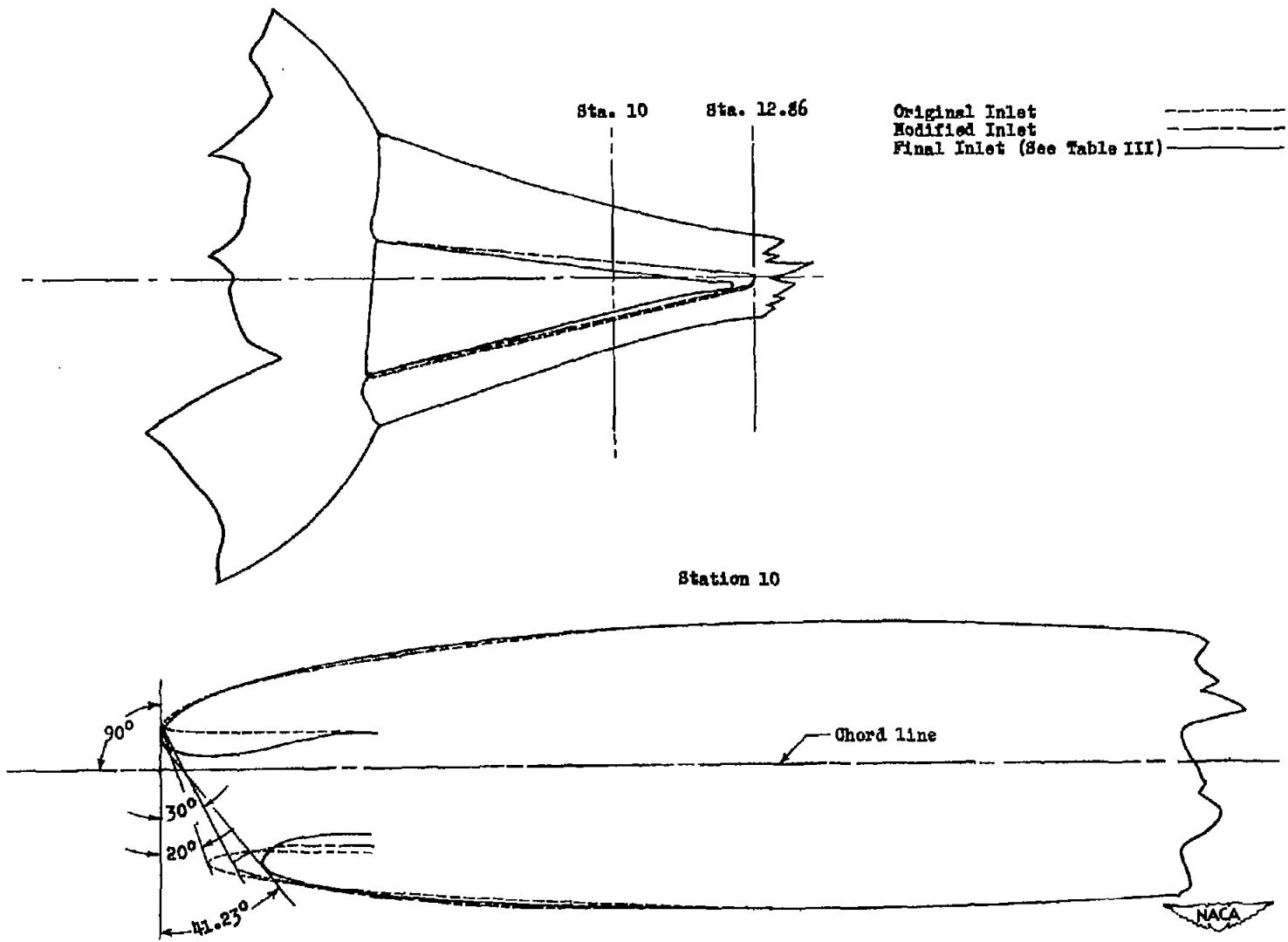


Figure 3.- Comparison of the three inlet nose shapes.

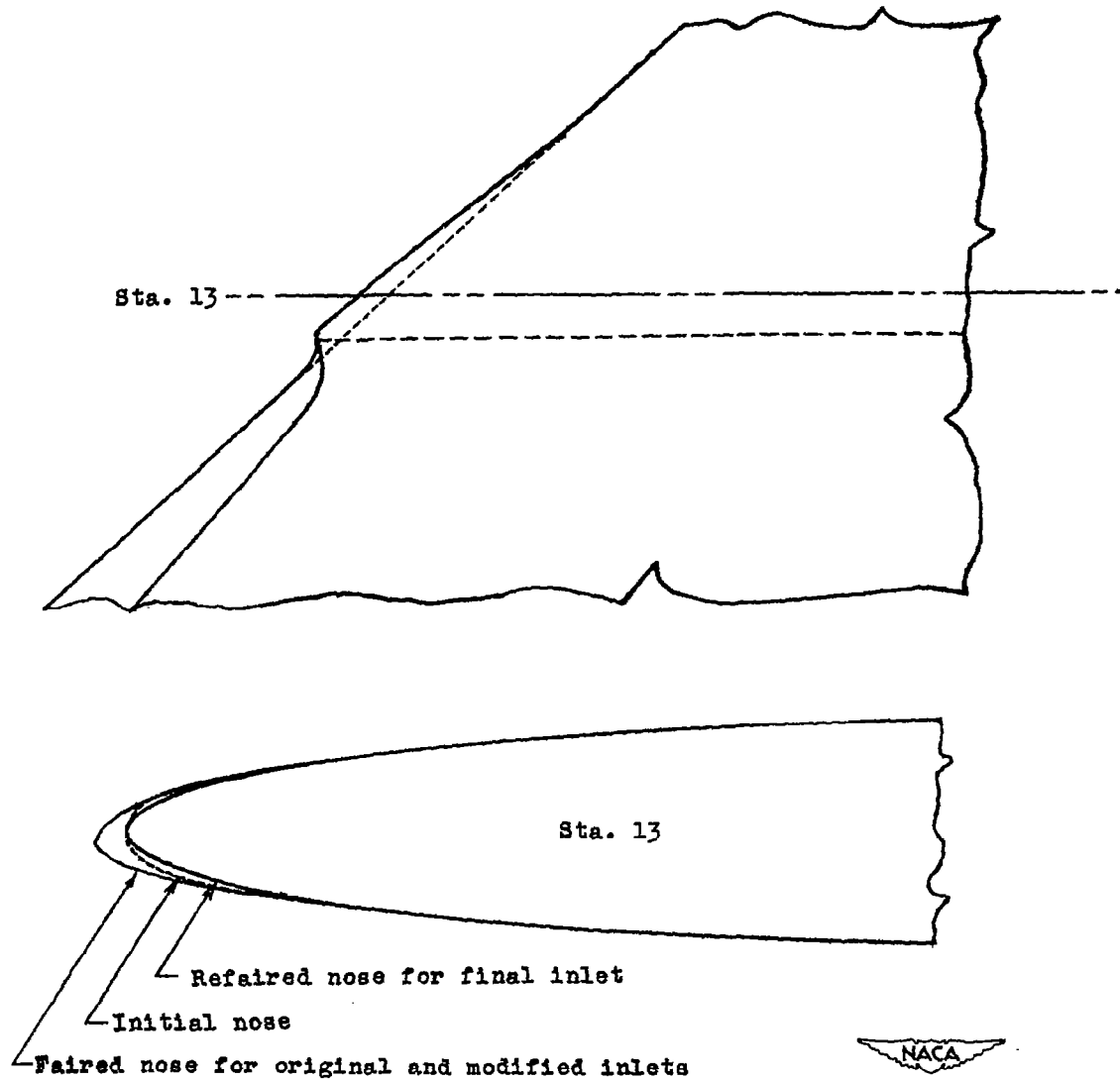
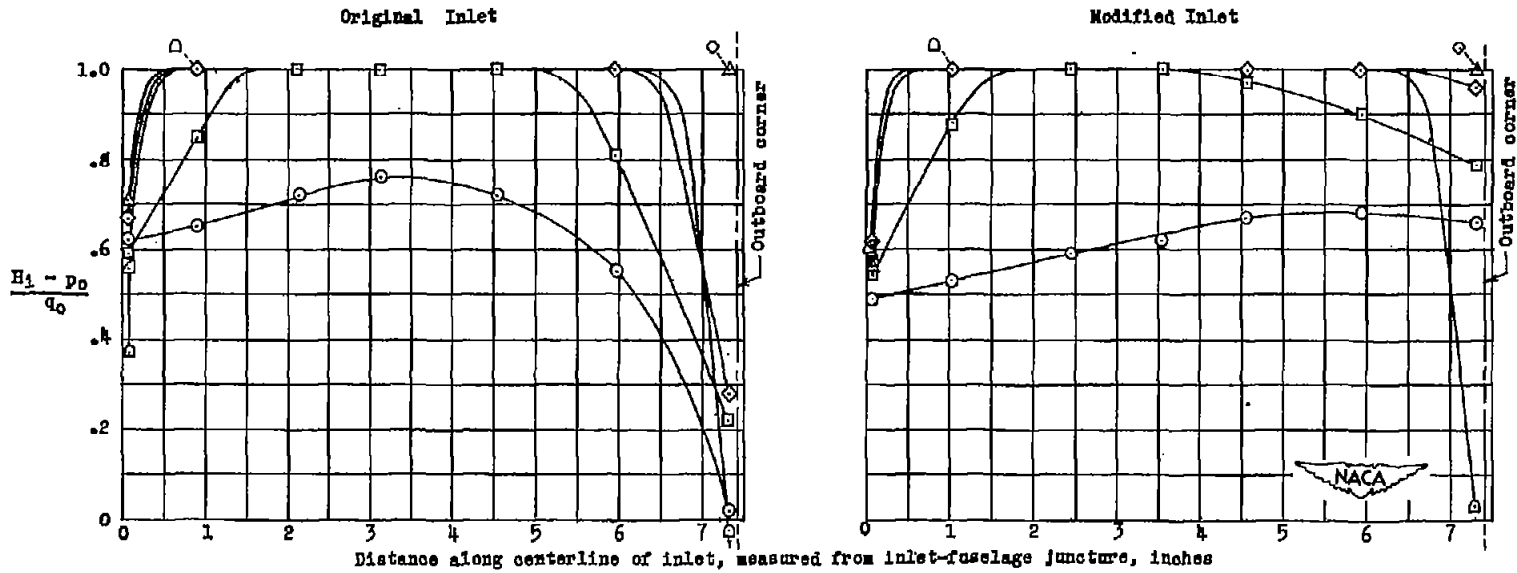
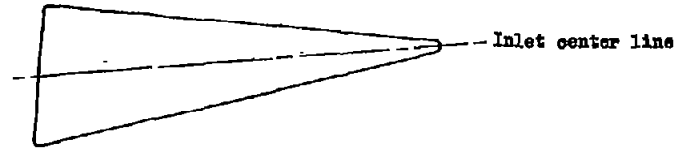


Figure 4.- Comparison of nose shapes at station 13 for the three inlets.

Symbol	$V_1/V_0$
○	0
□	.20
◇	.40
△	.59
▽	.79
◊	.99
◓	1.19
◔	1.50



(a) Inlet center line,  $\alpha = 0^\circ$ .

Figure 5.- Inlet total-pressure distributions for the original and modified inlets.

Symbol	$V_1/V_0$
○	0
□	.20
◇	.40
△	.59
▽	.79
◊	.99
◊	1.19
◊	1.50

Sta. 6.23

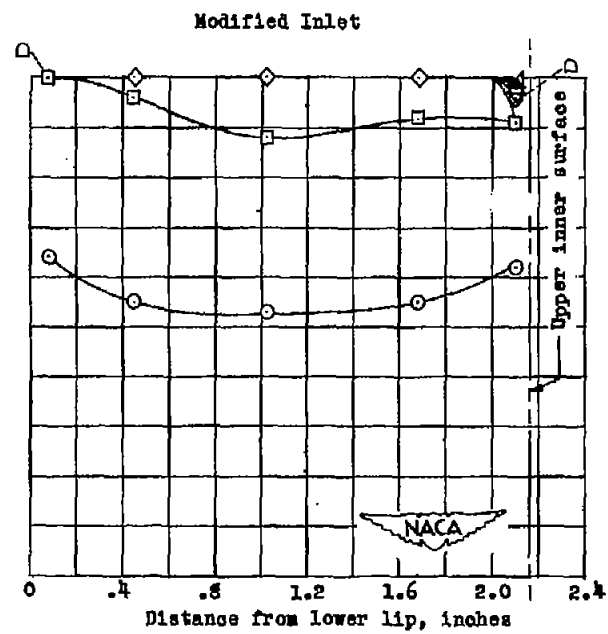
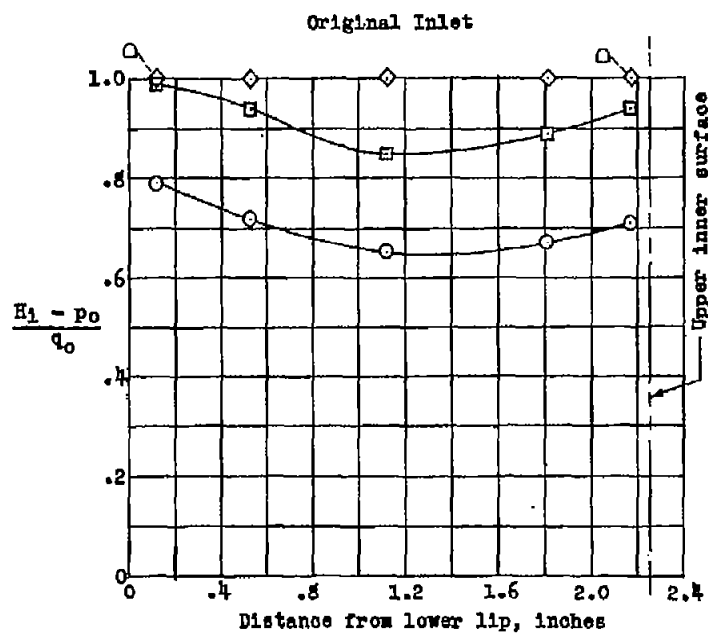
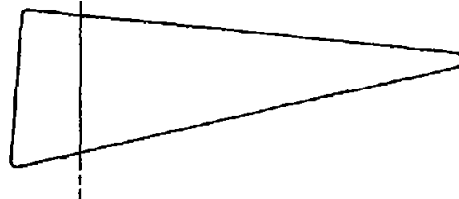
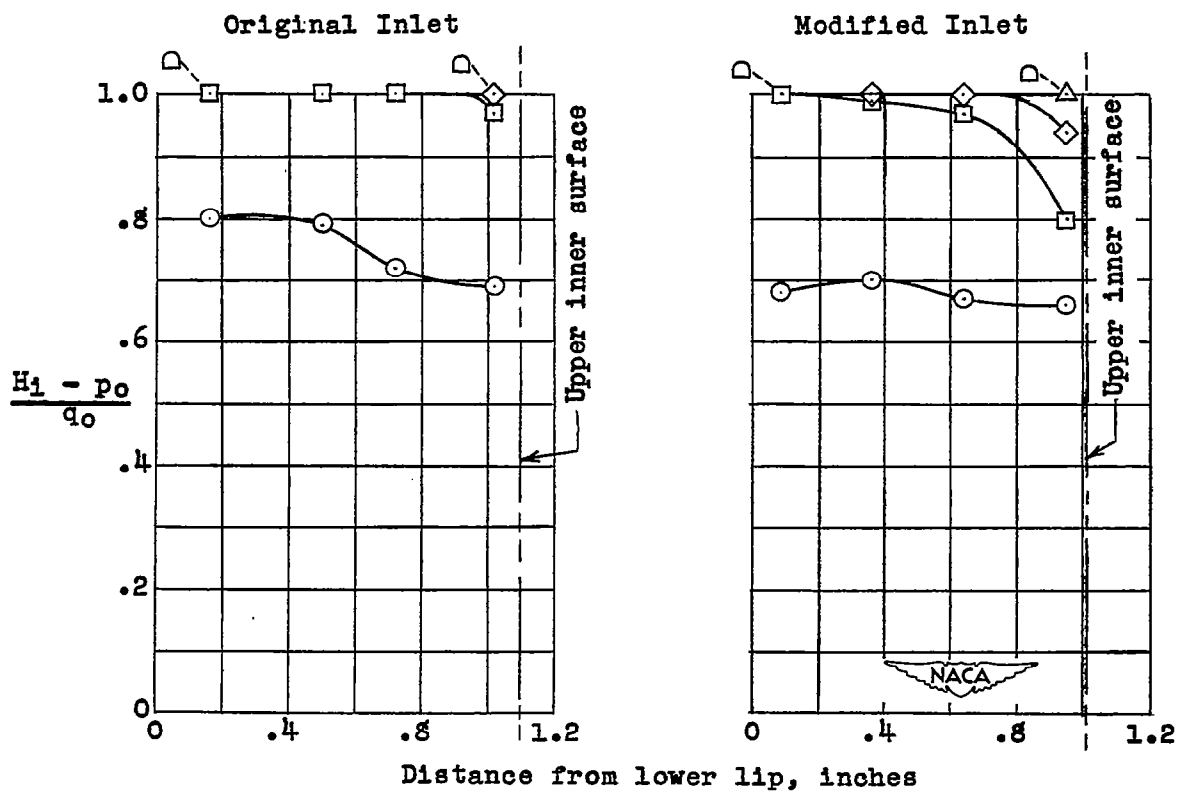
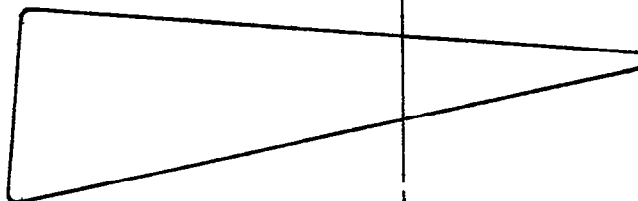
(b) Station 6.23,  $\alpha = 0^\circ$ .

Figure 5.- Continued.

Symbol	$V_1/V_0$
○	0
□	0.20
◇	.40
△	.59
▽	.79
◊	.99
◈	1.19
◉	1.50

Sta. 9.80

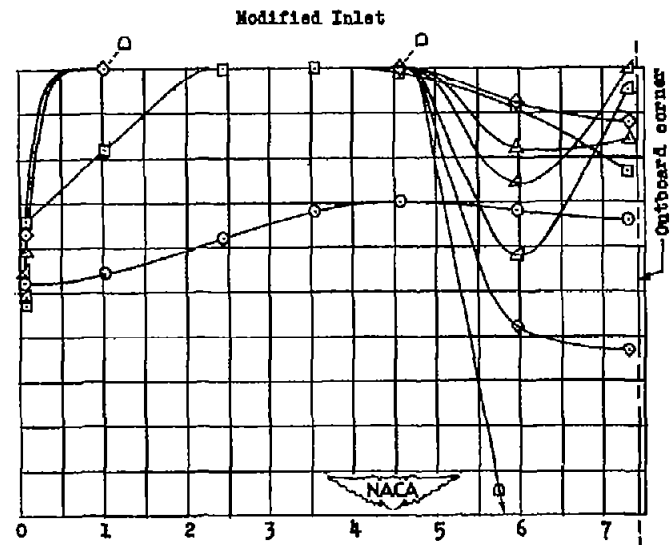
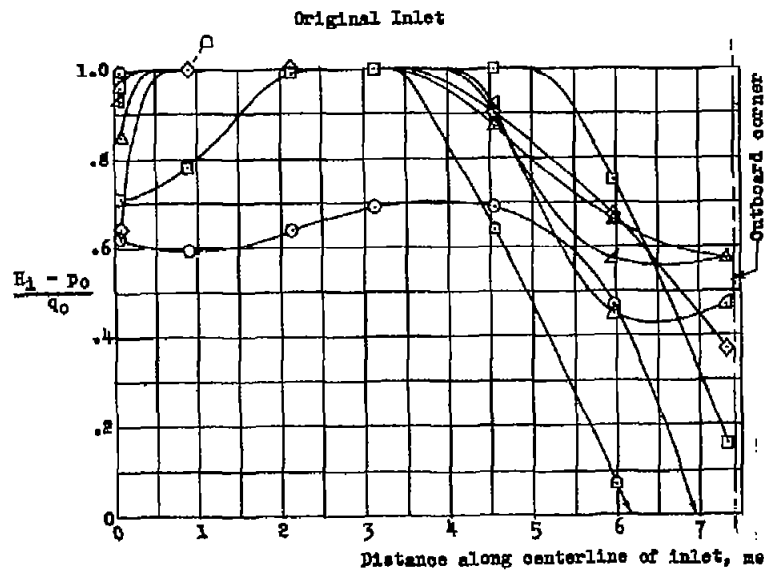
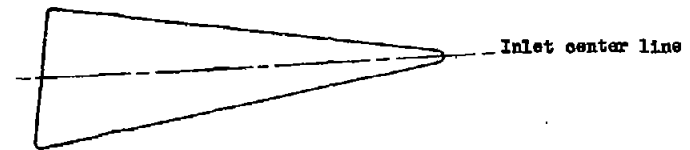


(c) Station 9.80,  $\alpha = 0^\circ$ .

Figure 5.- Continued.



Symbol	$V_1/V_0$
○	0
◇	.20
□	.40
△	.59
▽	.79
△	.99
◇	1.19
◇	1.50



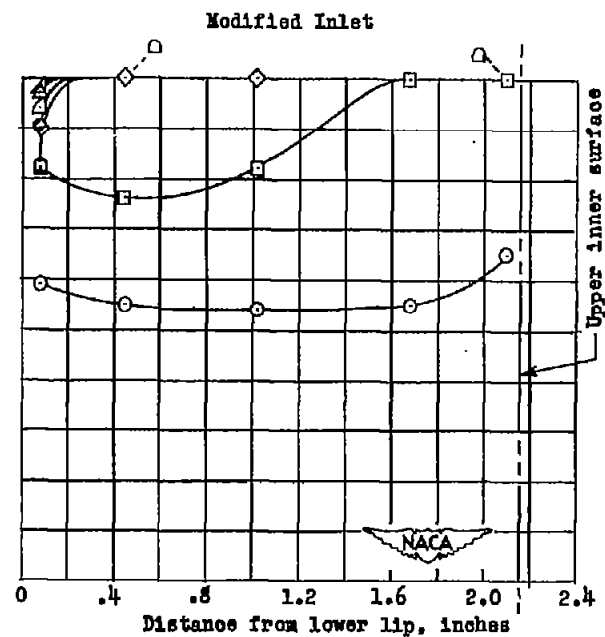
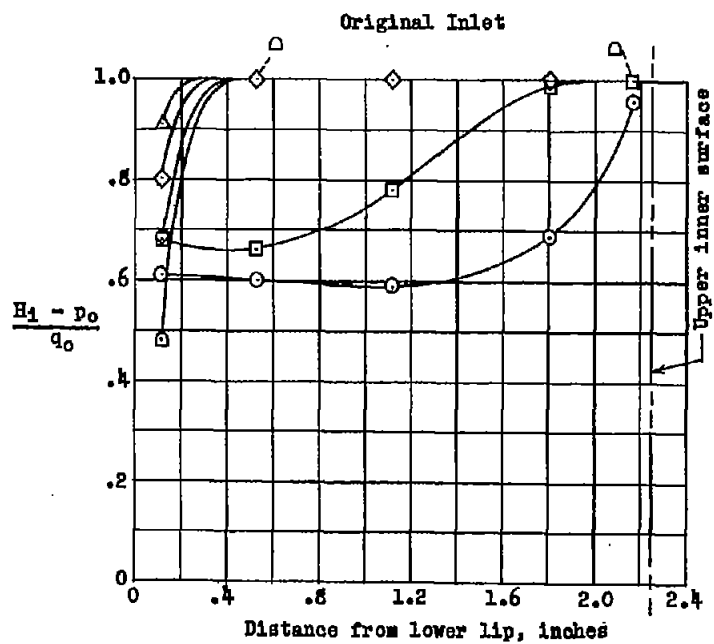
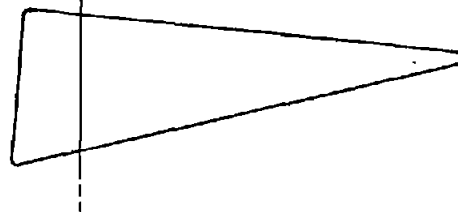
Distance along centerline of inlet, measured from inlet-fuselage juncture, inches

(d) Inlet center line,  $\alpha = 10^\circ$ .

Figure 5.- Continued.

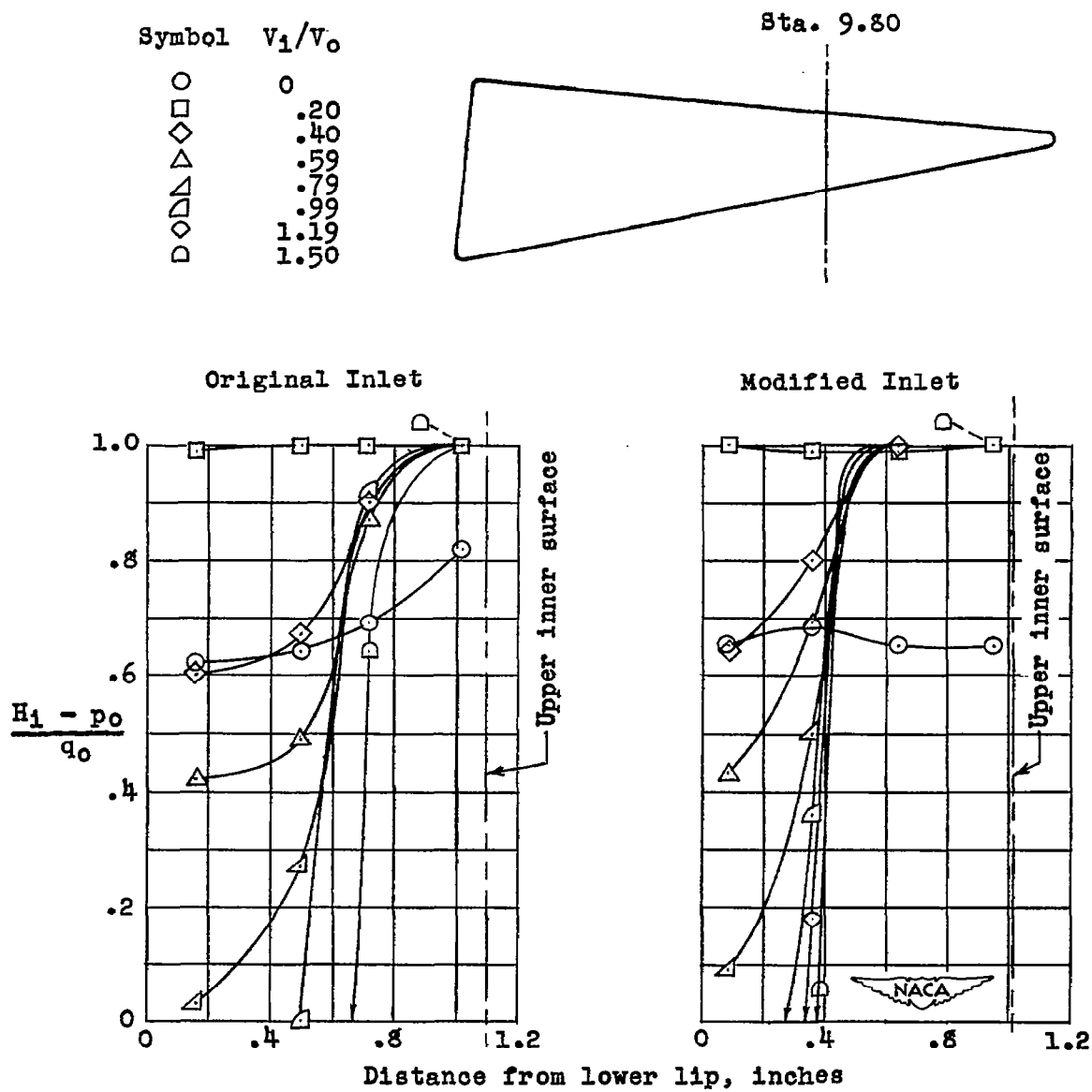
Symbol	$V_1/V_0$
○	0
□	.20
◇	.40
△	.59
▴	.79
◇	.99
◇	1.19
◇	1.50

Sta. 6.23



(e) Station 6.23,  $\alpha = 10^\circ$ .

Figure 5.- Continued.



(f) Station 9.80,  $\alpha = 10^\circ$ .

Figure 5.- Concluded.

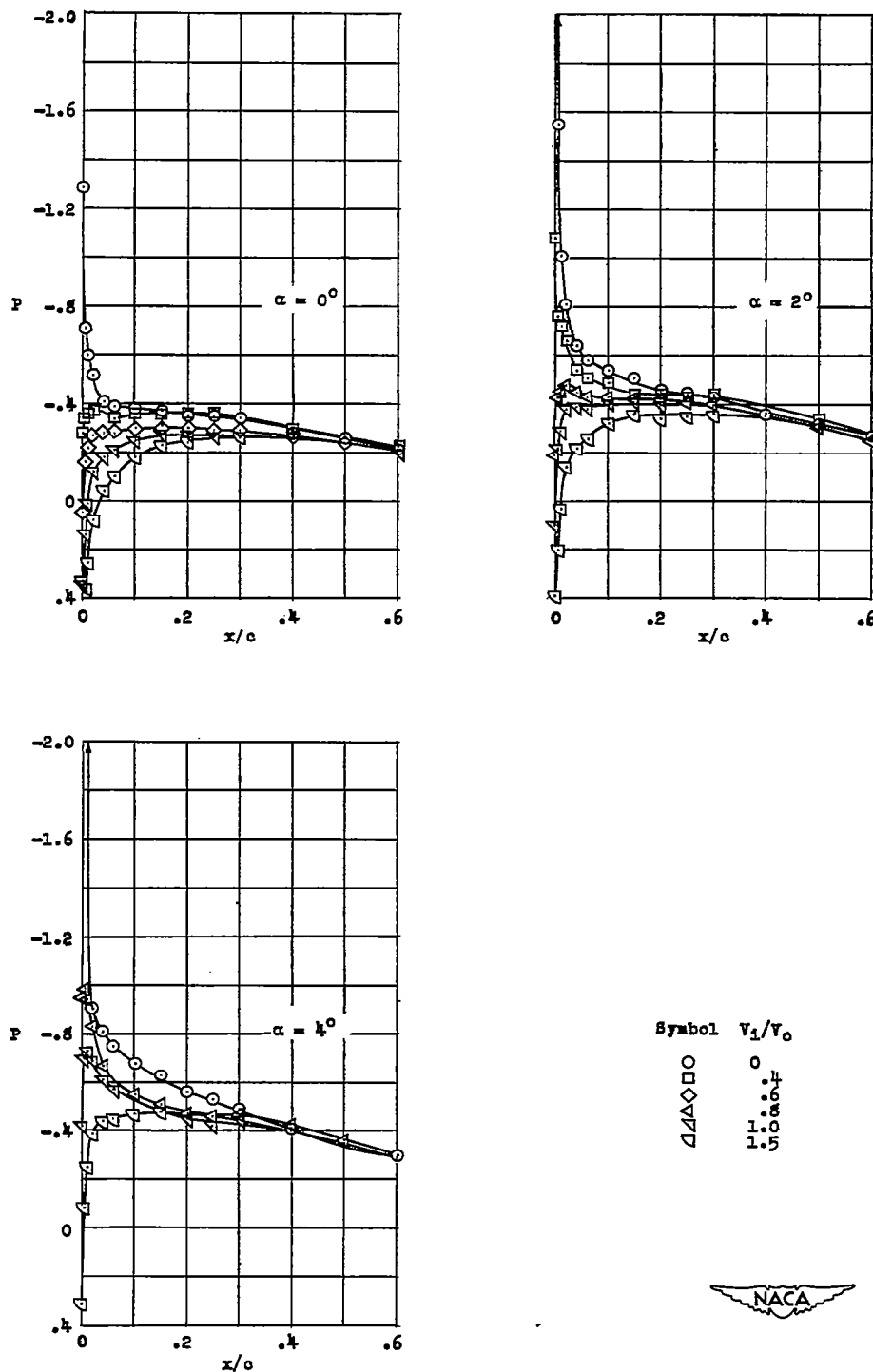


Figure 6.- Static-pressure distribution over the upper surface at station 10 of the original inlet.

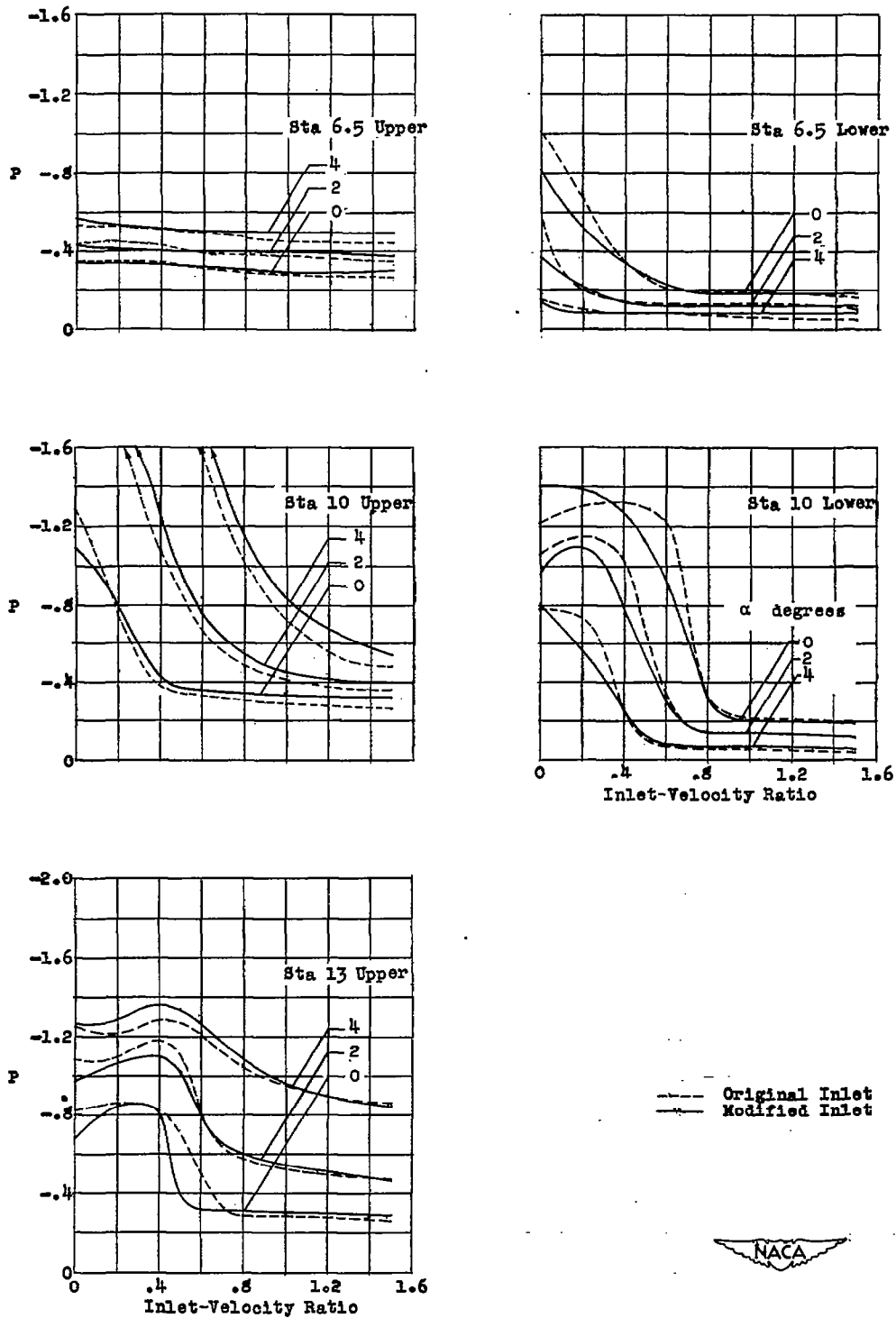
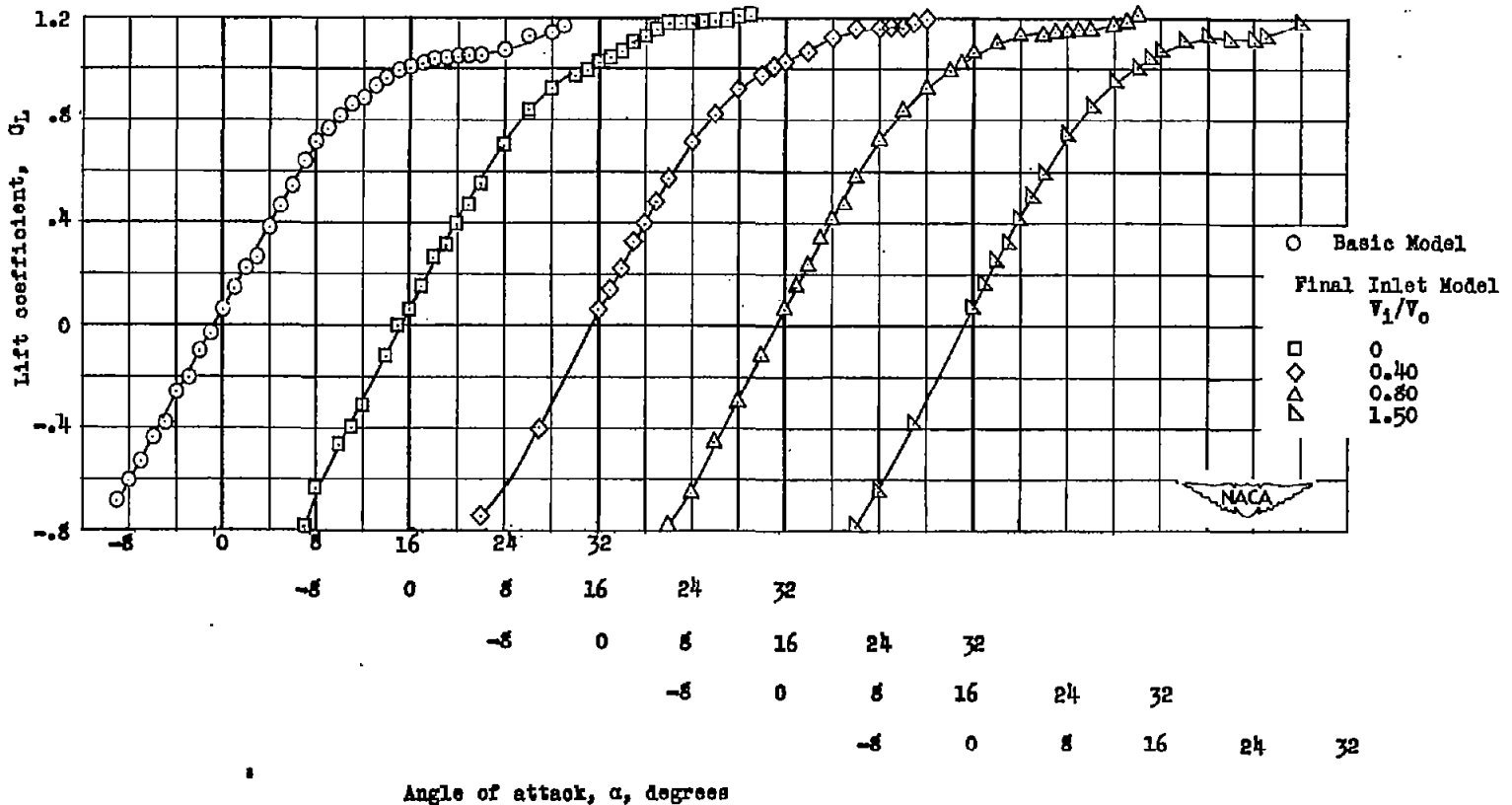
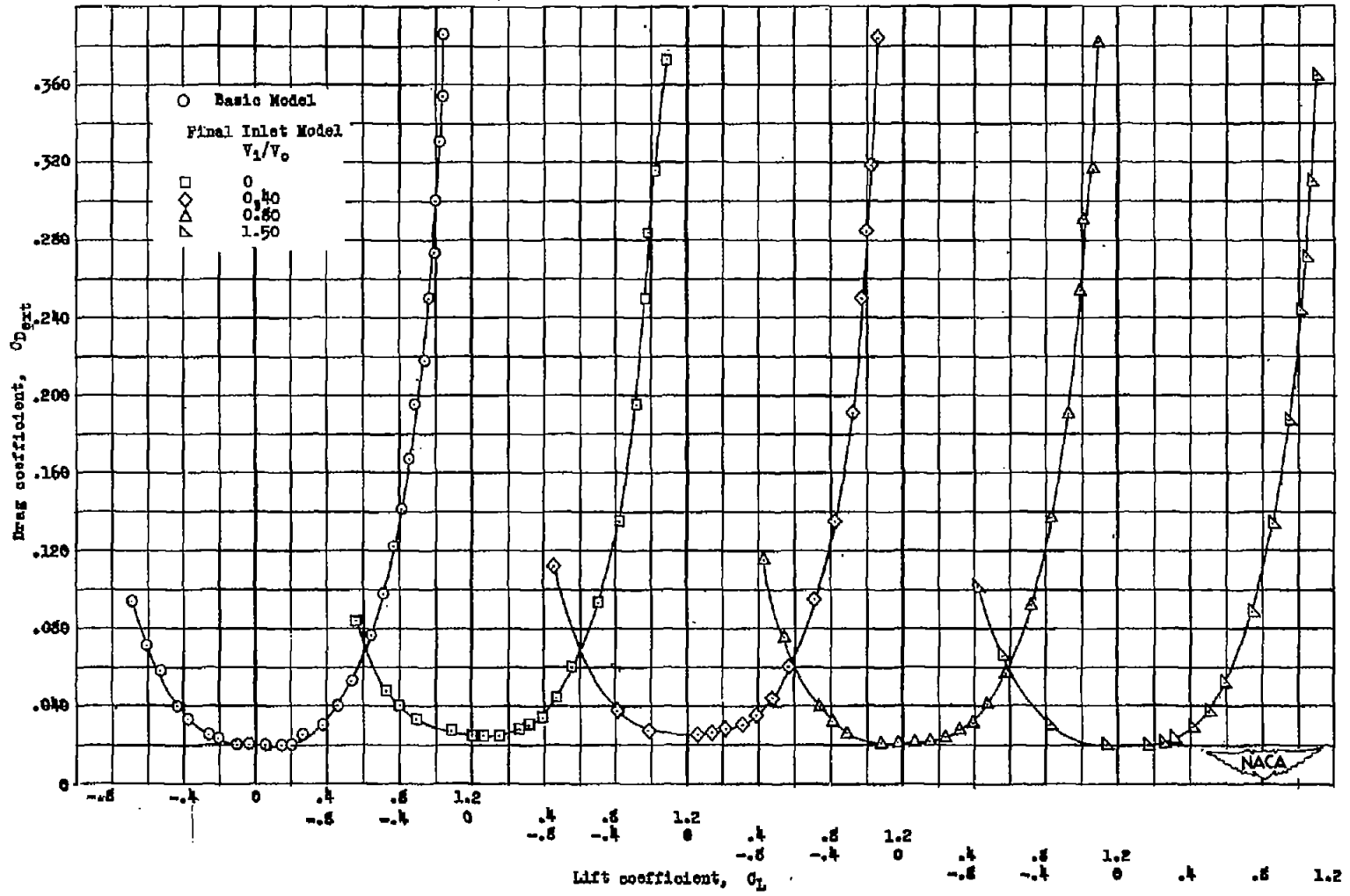


Figure 7.- Minimum external surface-pressure coefficients at the several measuring stations for the original and modified inlets.



(a) Lift.

Figure 8.- Comparison of aerodynamic forces of the basic wing model and the final inlet model at several inlet-velocity ratios.



(b) Drag.

Figure 8.- Concluded.

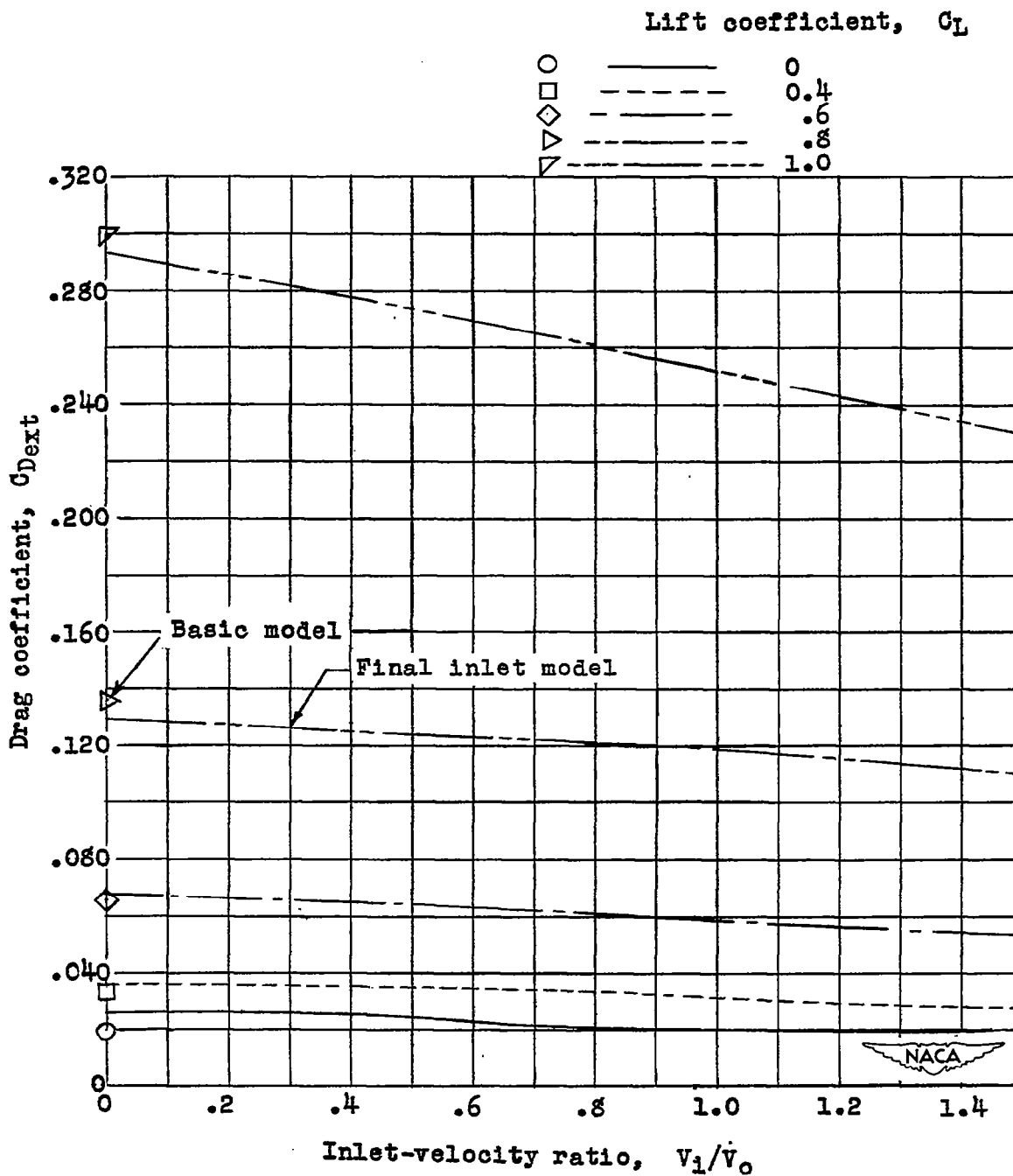
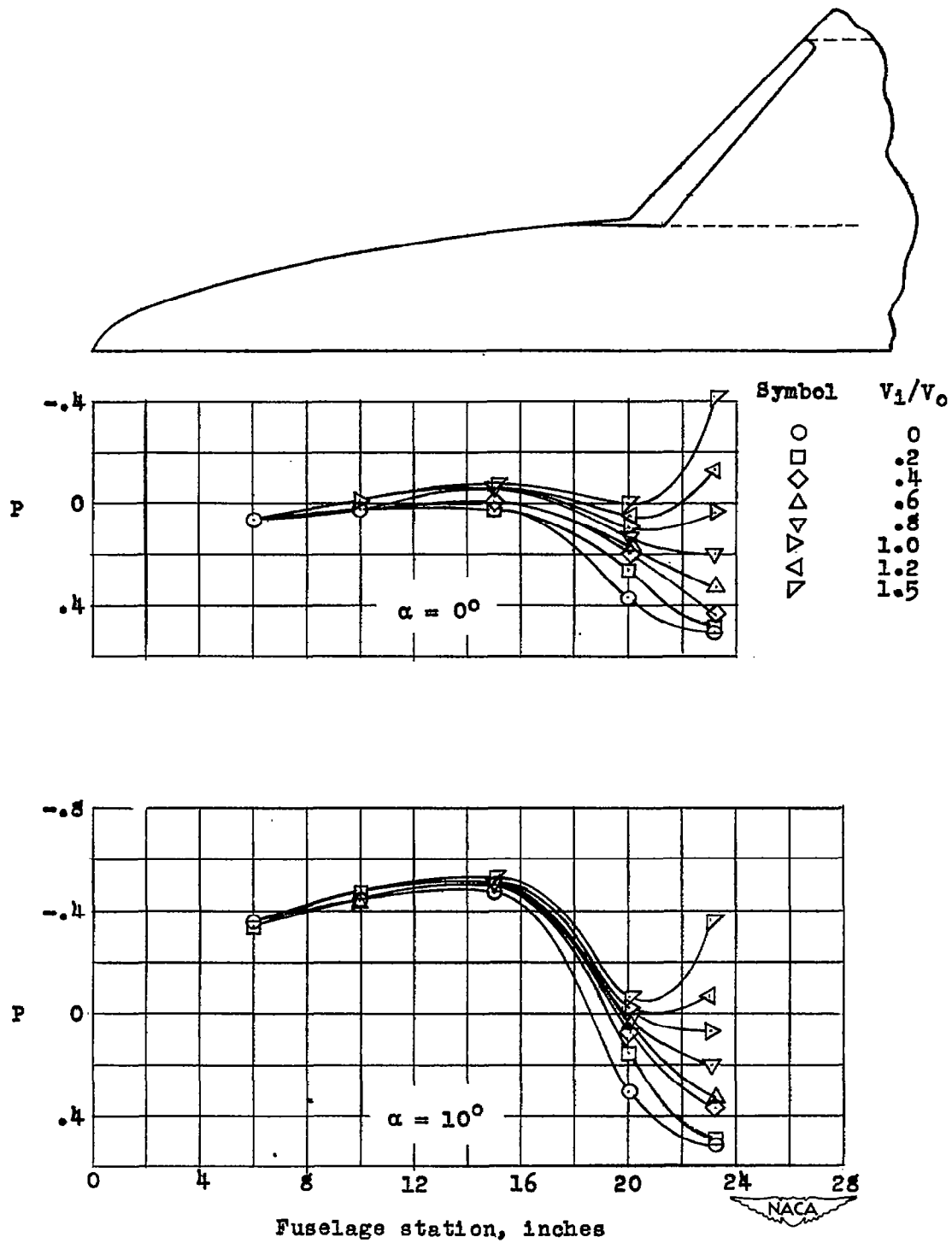


Figure 9.- Effect of inlet-velocity ratio on the external drag coefficient of the final inlet model.





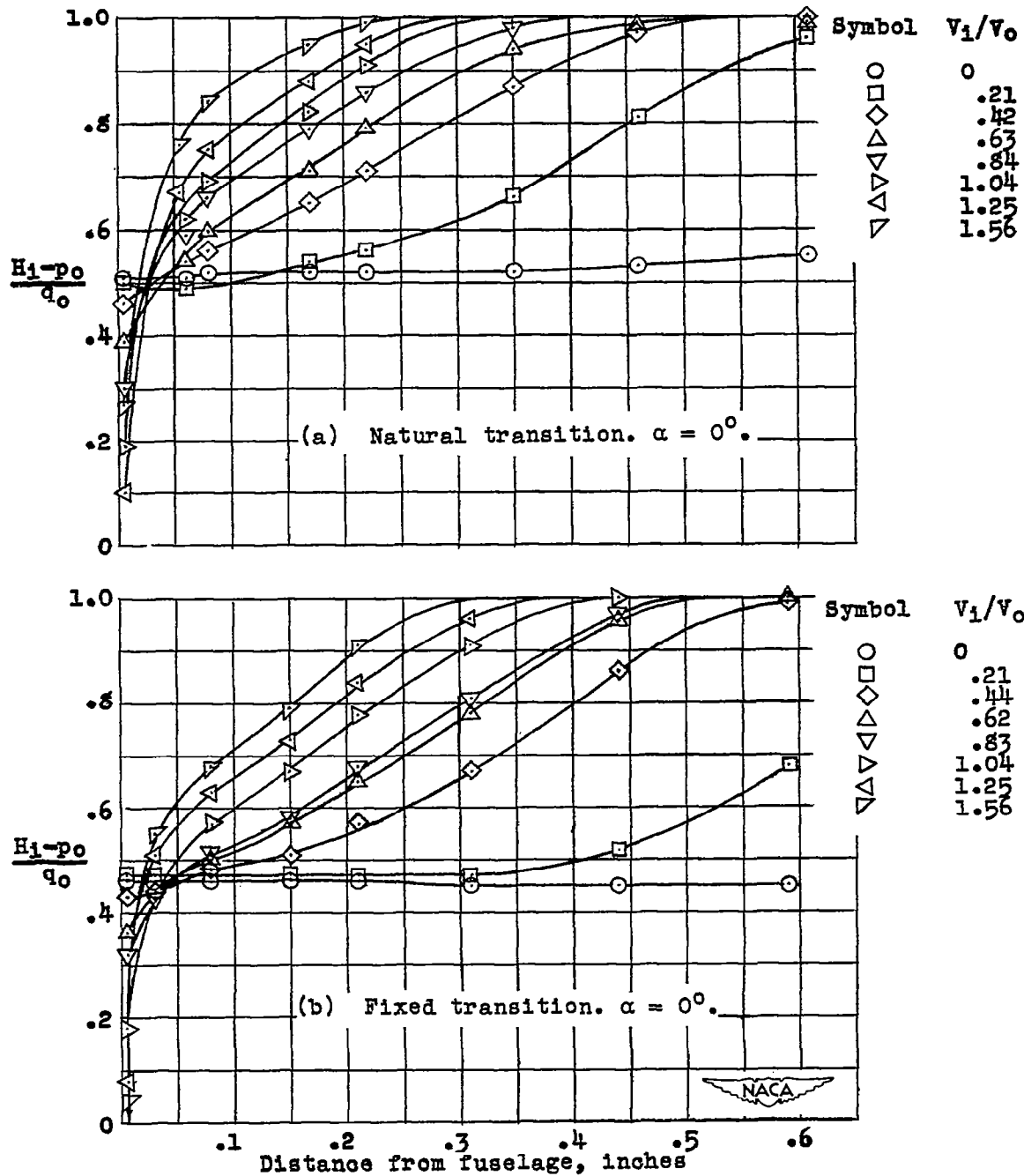


Figure 11.- Total-pressure distribution in fuselage boundary layer of final inlet model measured just inside inlet (station 23.15 inches) in plane of wing chord.

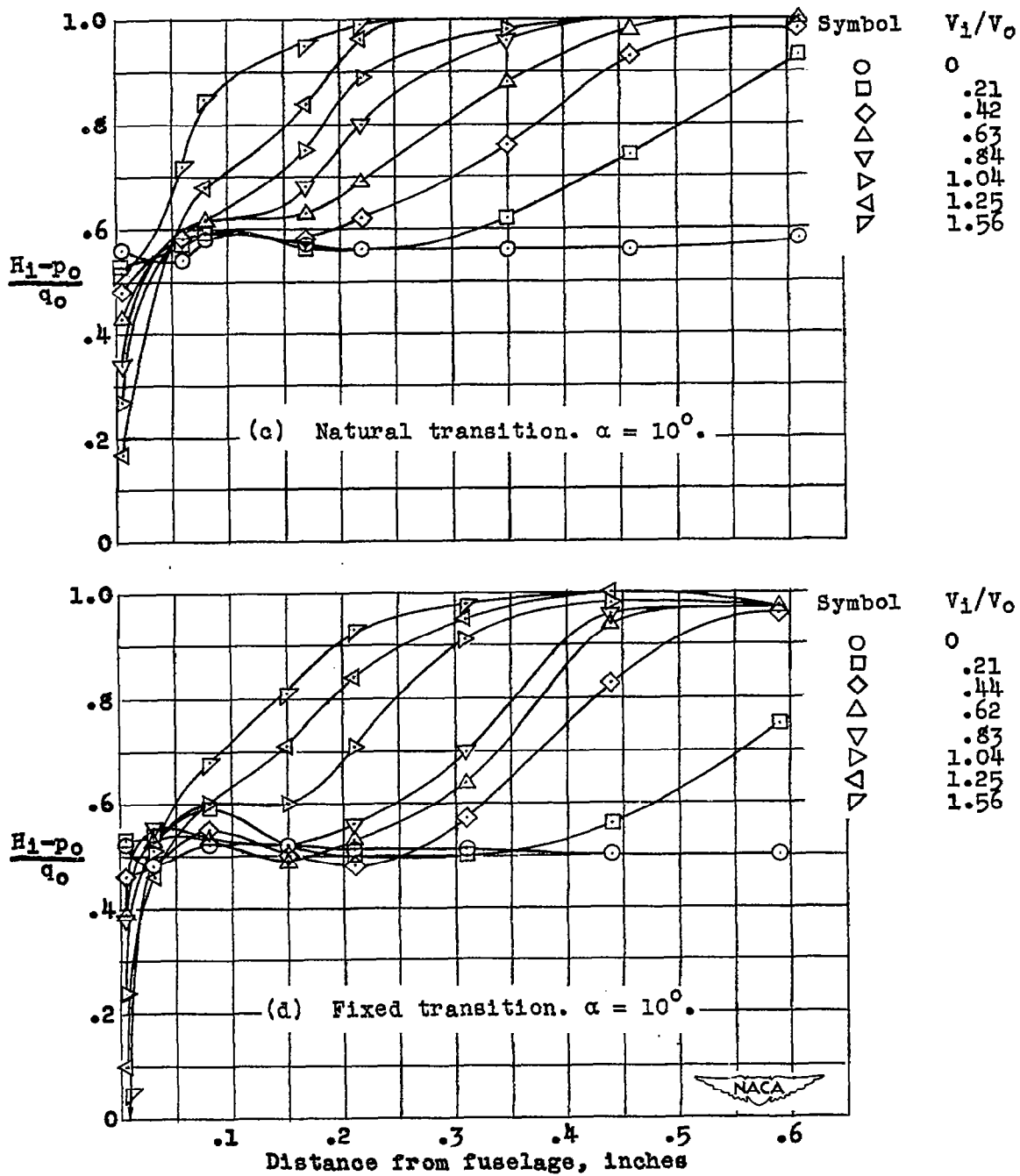


Figure 11.- Concluded.

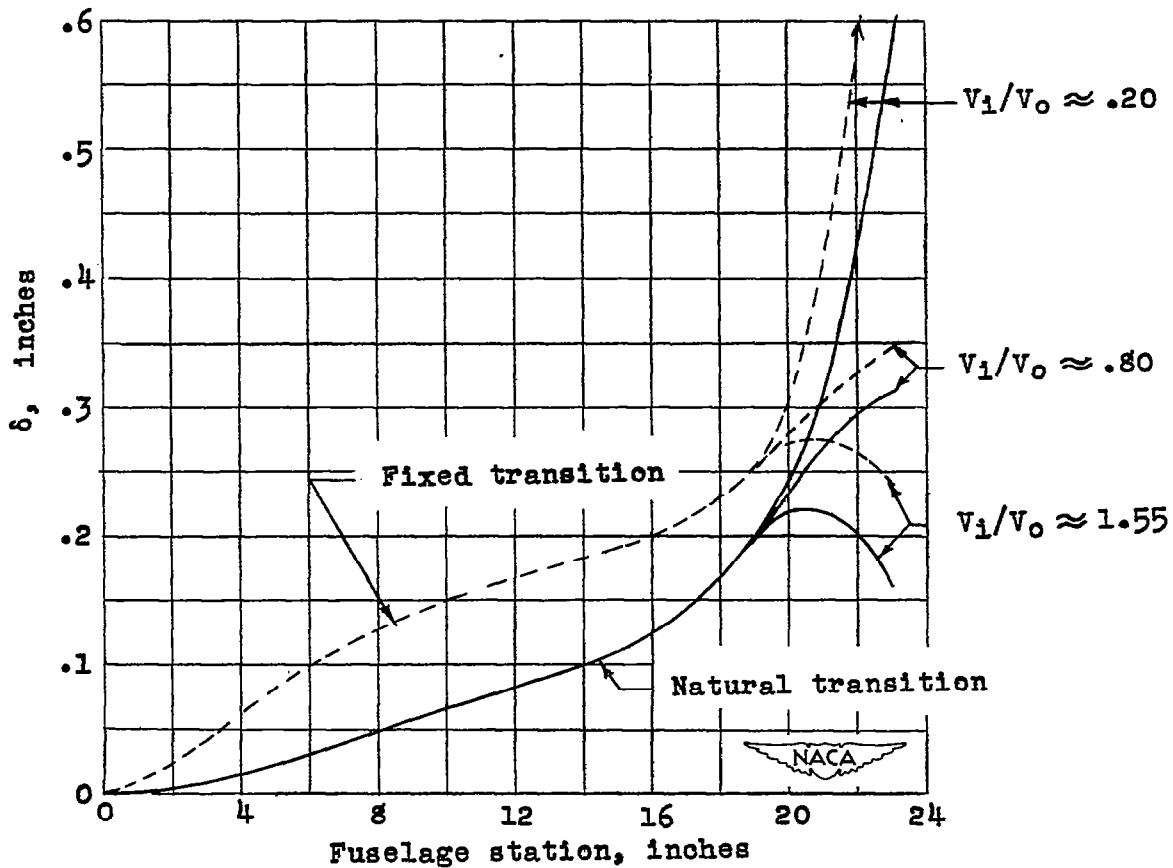
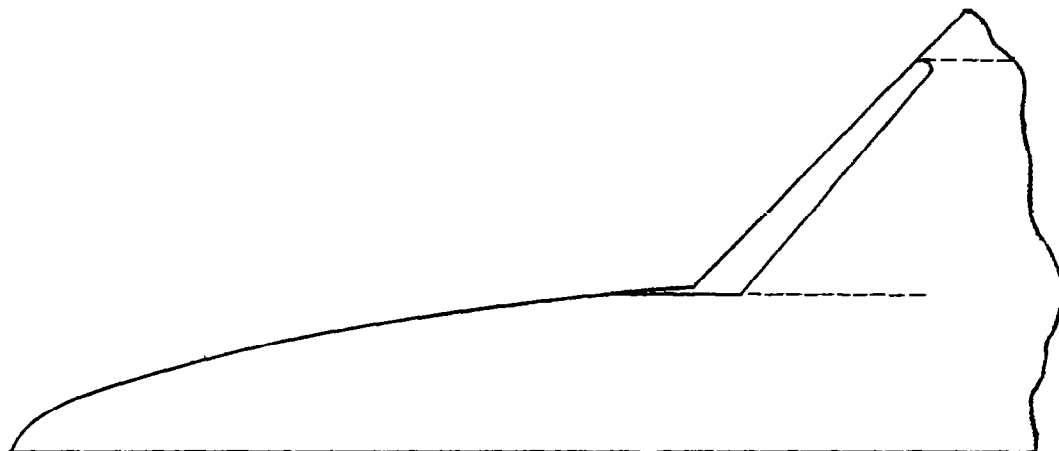


Figure 12.- Growth of fuselage boundary layer measured in the plane of the wing chord of the final inlet model,  $\alpha = 0^\circ$ .

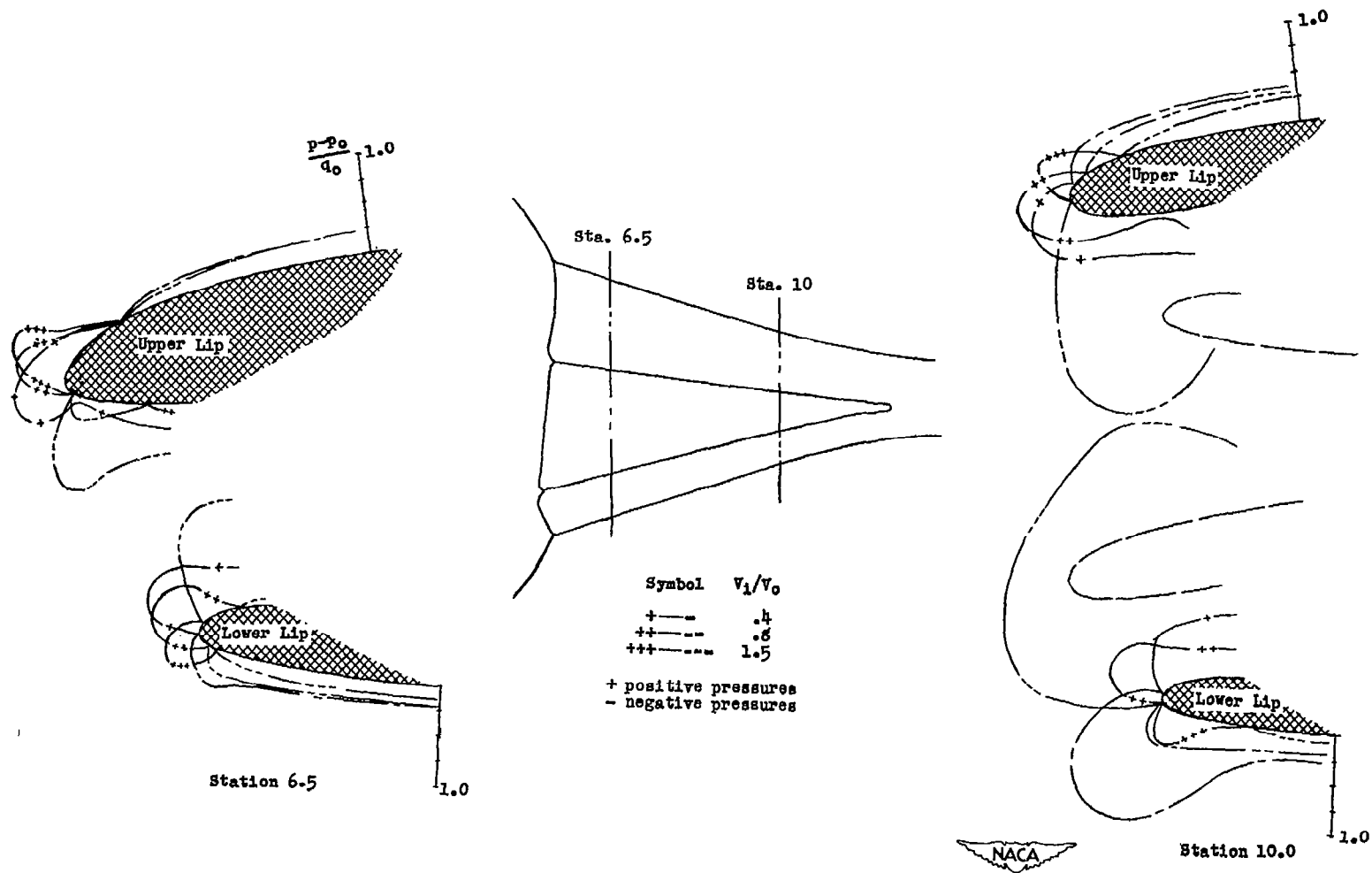


Figure 13.- Static-pressure distributions around inlet nose sections of final inlet model,  $\alpha = 0^\circ$ .

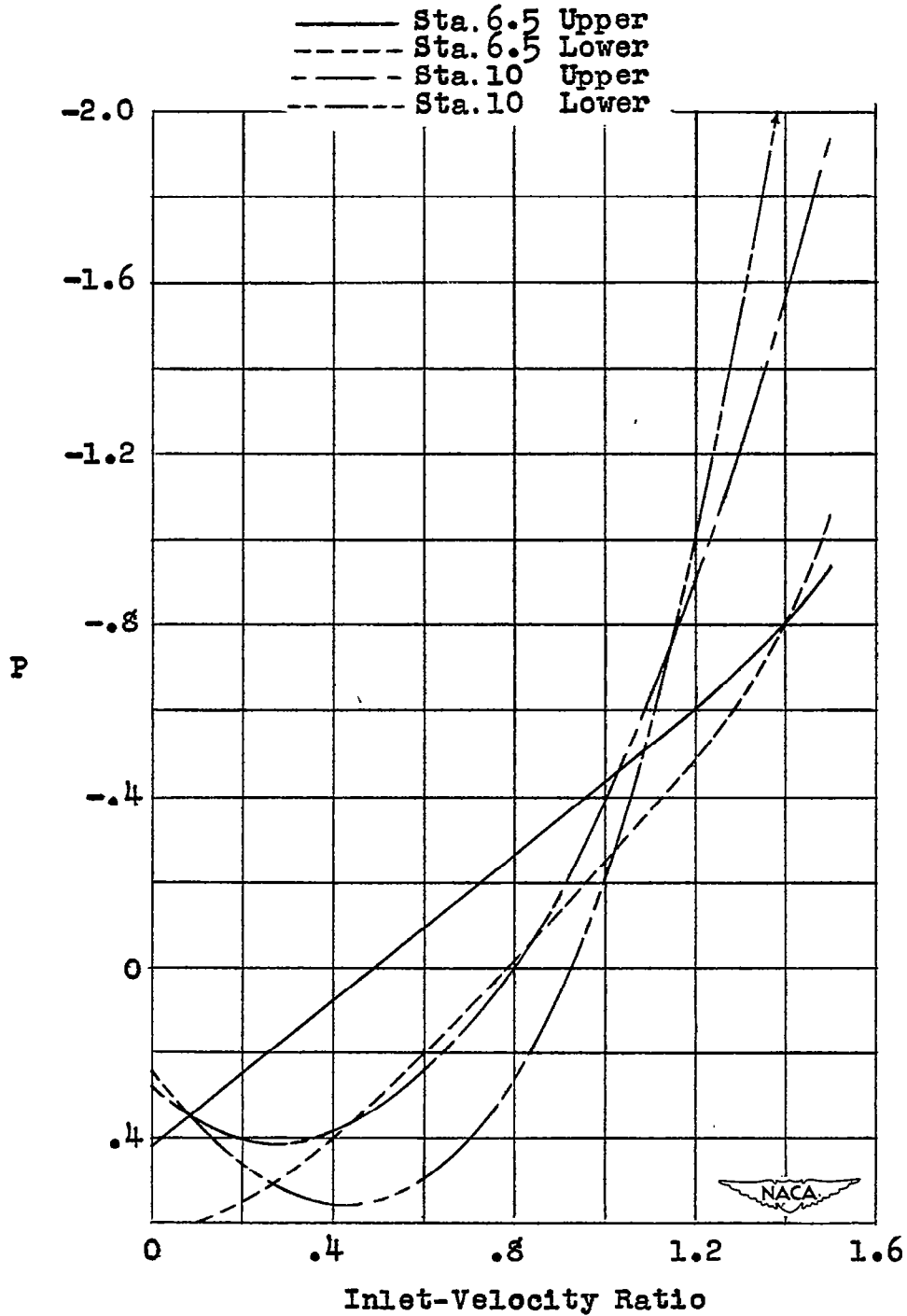
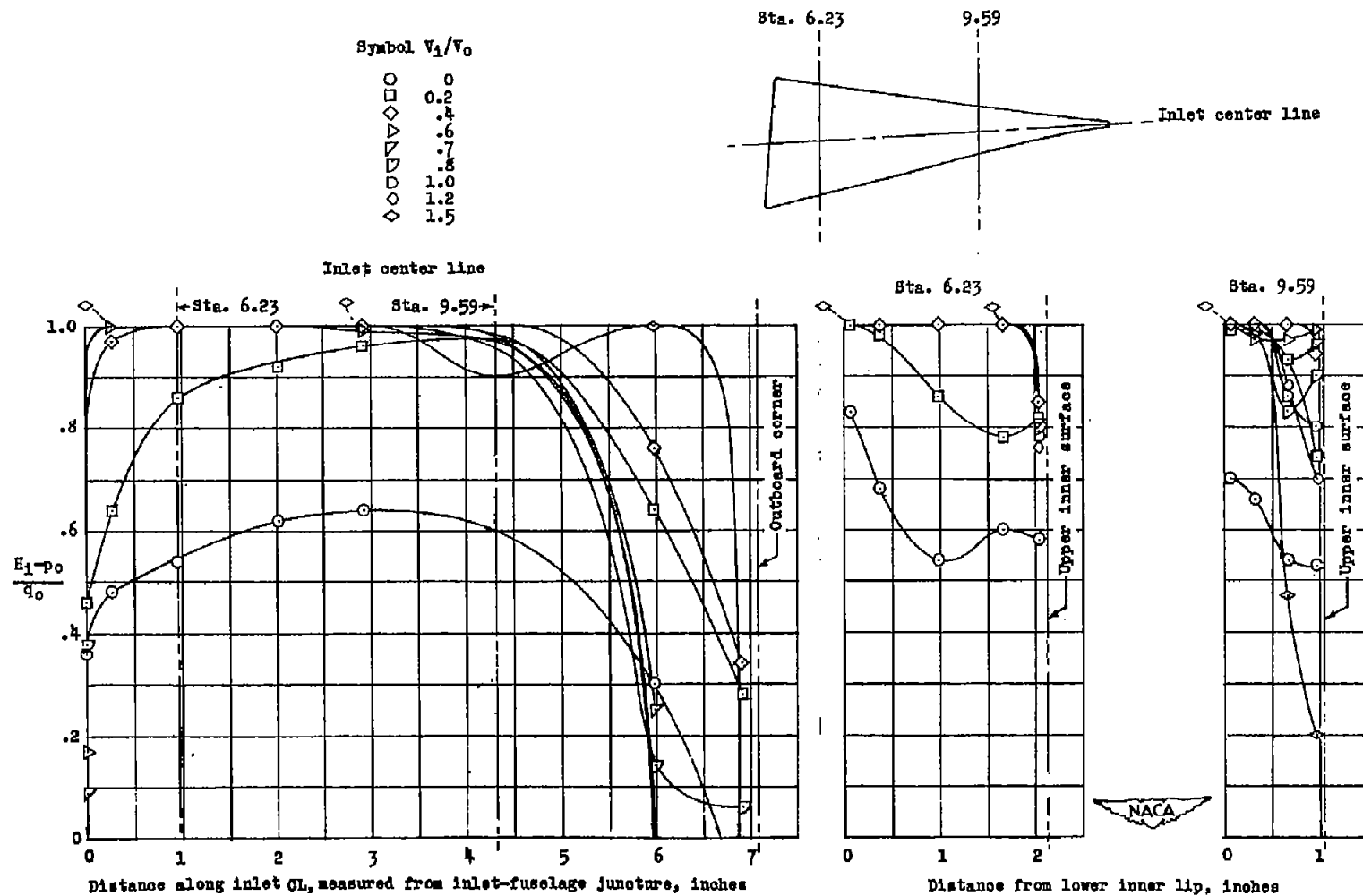


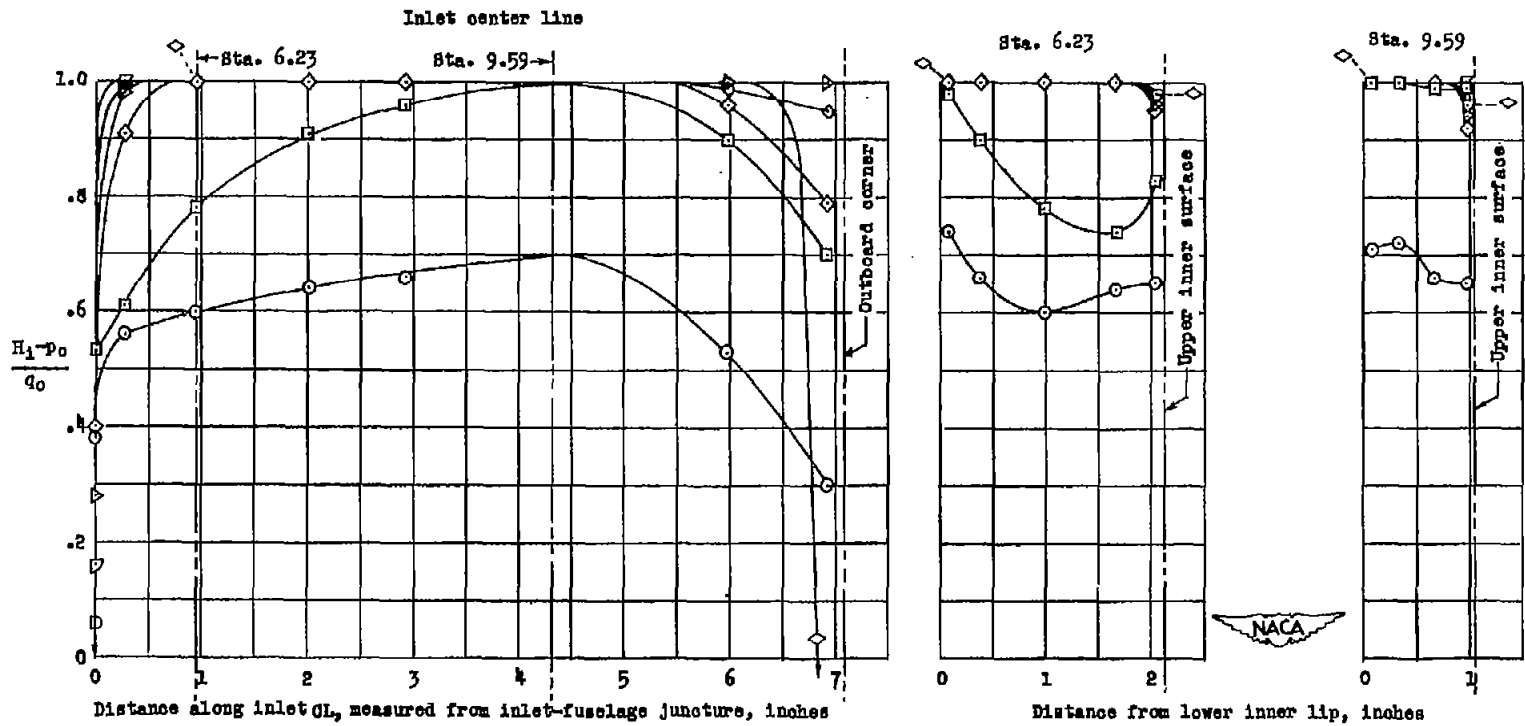
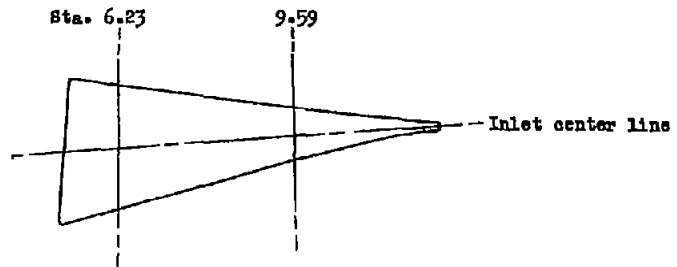
Figure 14.- Minimum static-pressure coefficients for inner-lip surfaces at the several inlet measuring stations of the final inlet model,  $\alpha = 0^\circ$ .



(a)  $\alpha = -5^\circ$ ,  $C_L \approx -0.39$ .

Figure 15.- Total-pressure distributions in inlet of the final inlet model.

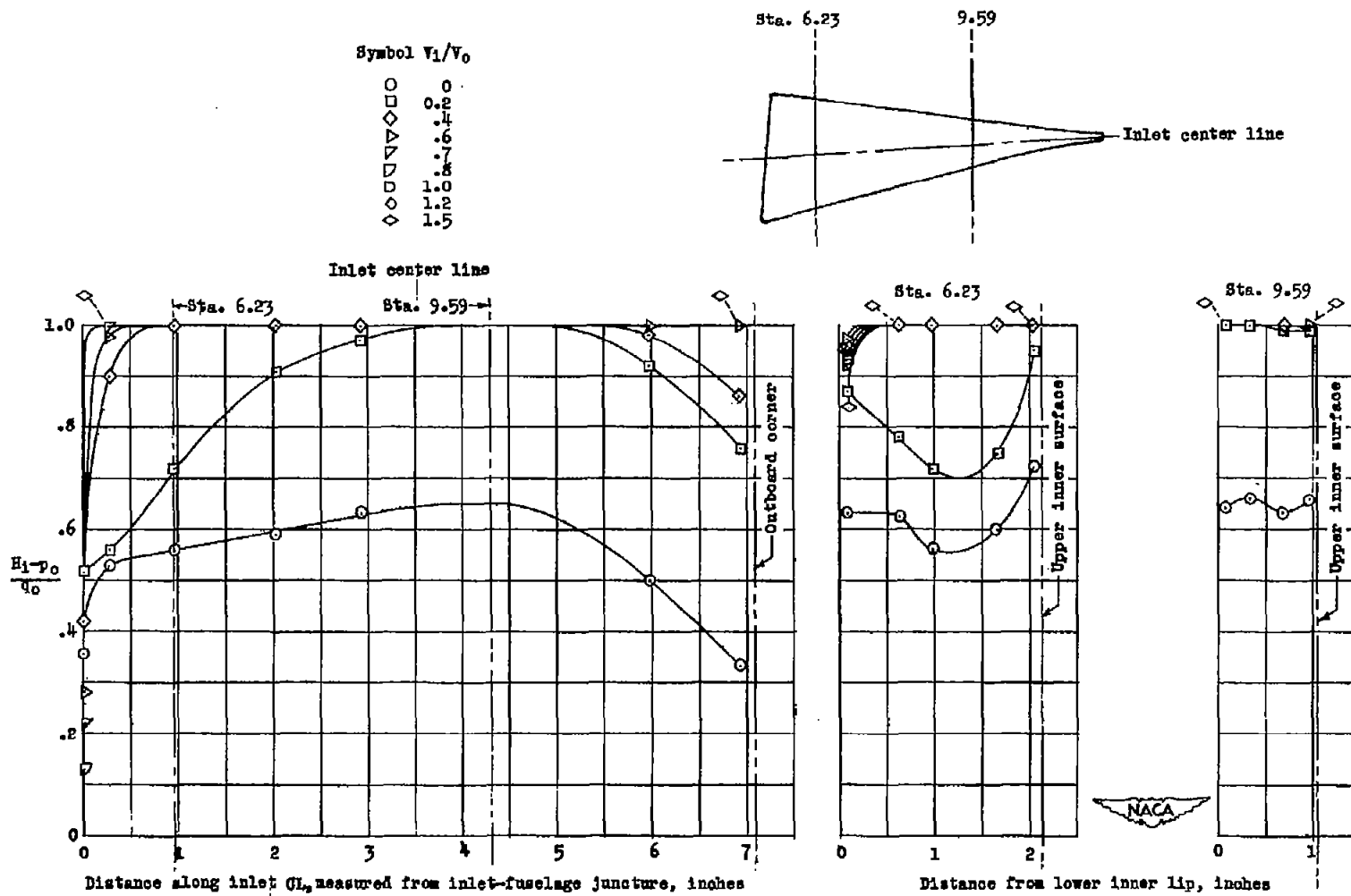
Symbol	$V_1/V_0$
○	0
◇	0.2
□	.4
△	.6
▽	.7
◇	.8
◇	1.0
◇	1.2
◇	1.5



(b)  $\alpha = 0^\circ$ ,  $C_L \approx 0.06$ .

Figure 15.- Continued.



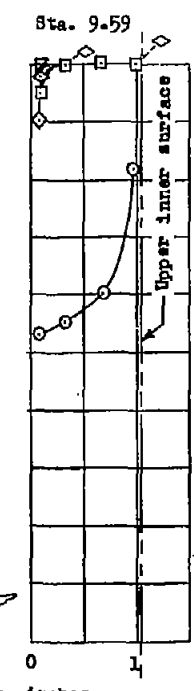
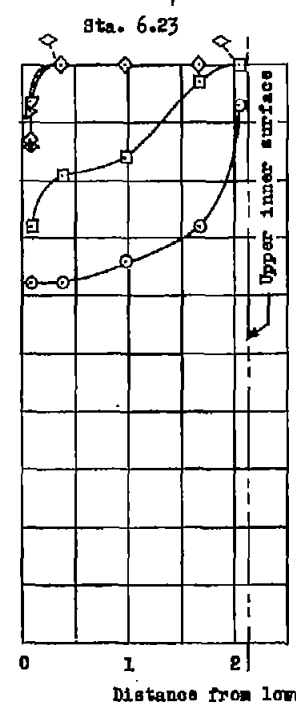
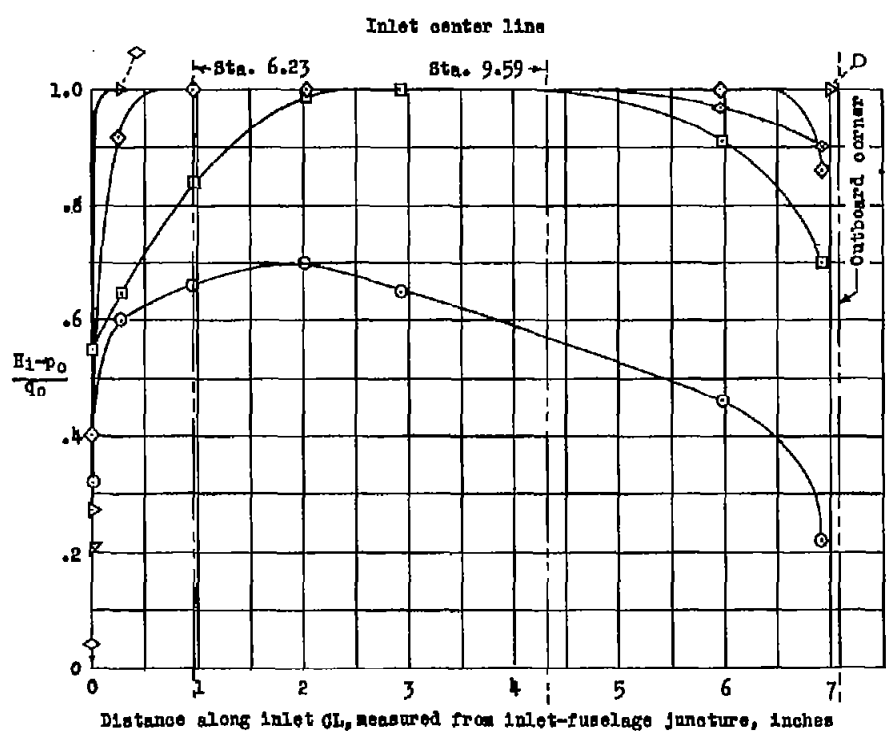
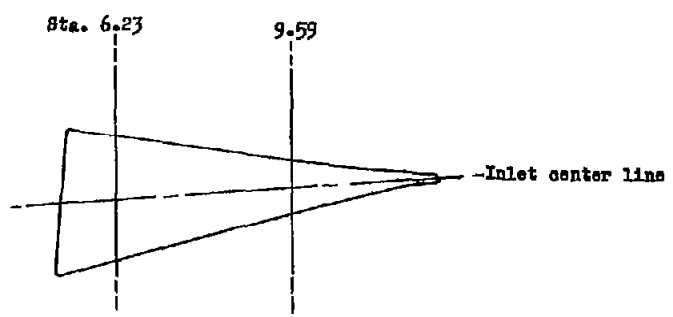


(c)  $\alpha = 5^\circ$ ,  $C_L \approx 0.47$ .

Figure 15.- Continued.

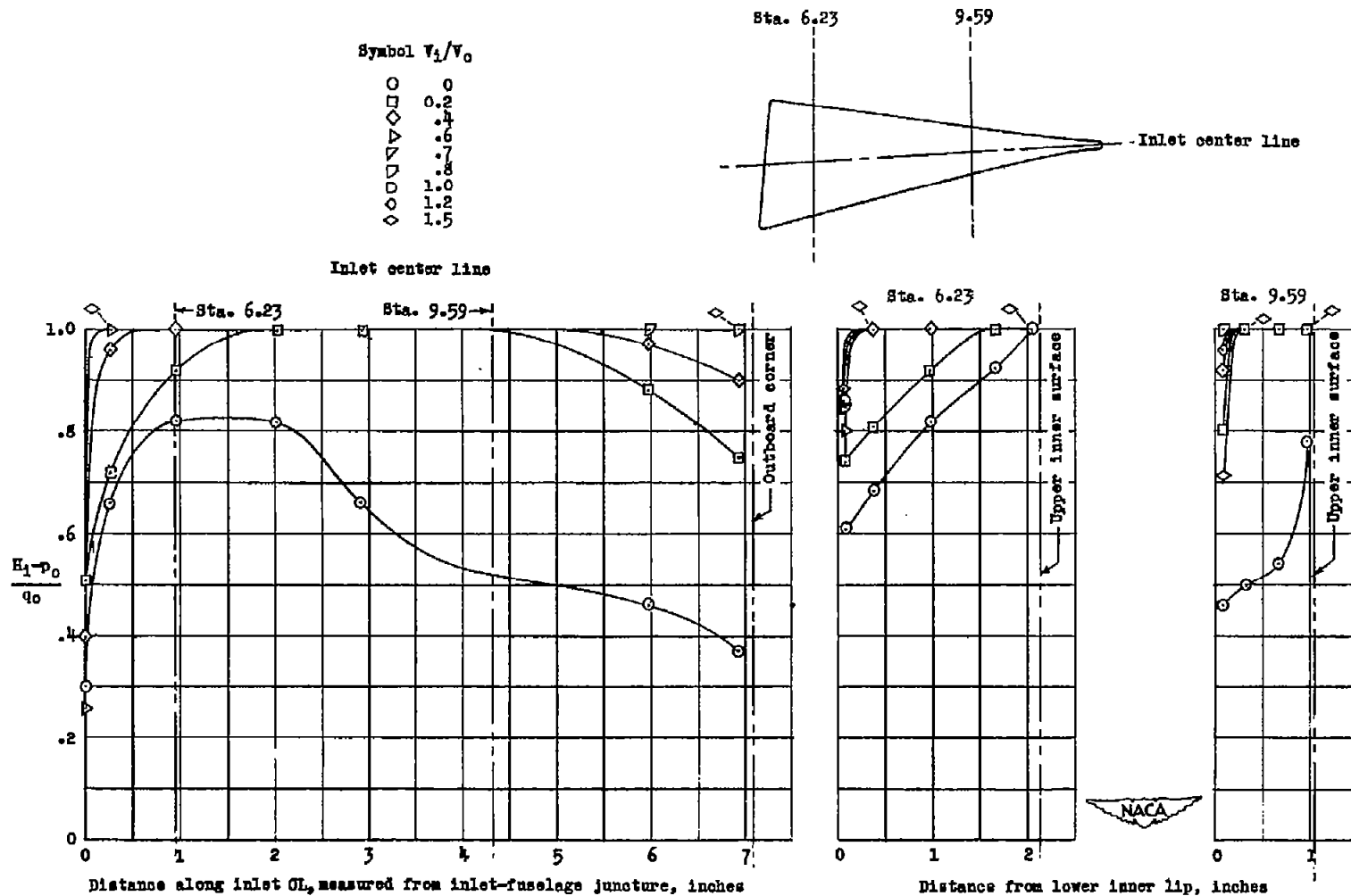
Symbol  $V_1/V_0$

○	0
□	0.2
◇	0.4
△	0.6
▽	0.7
◇	0.8
□	1.0
◇	1.2
◇	1.5



(d)  $\alpha = 10^\circ$ ,  $C_L \approx 0.83$ .

Figure 15.- Continued.



(e)  $\alpha = 12^\circ$ ,  $C_L \approx 0.92$ .

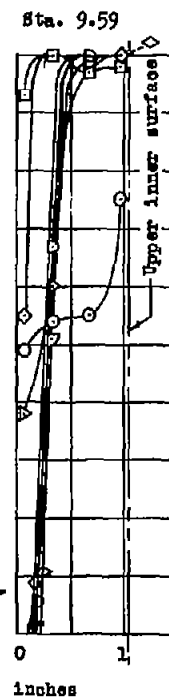
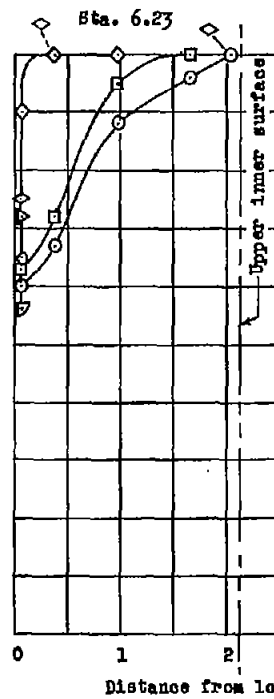
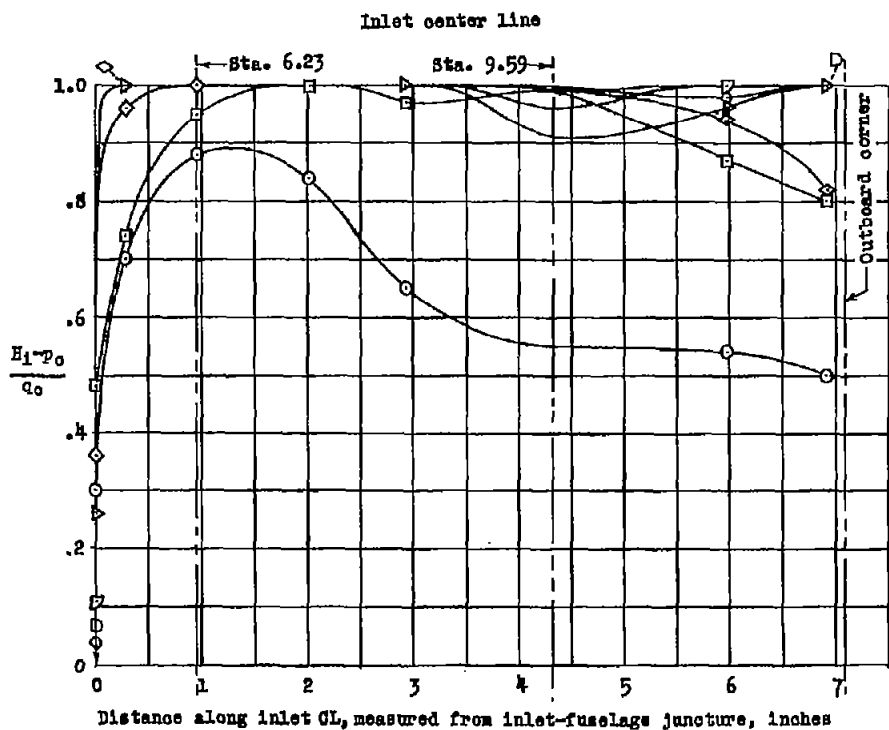
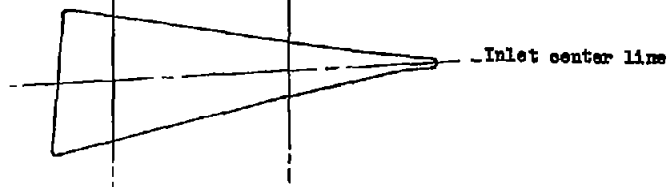
Figure 15.- Continued.

Symbol  $V_1/V_0$

- 0
- 0.2
- ◇ 0.4
- ▽ 0.6
- △ 0.7
- ▽ 0.8
- 1.0
- 1.2
- ◇ 1.5

Sta. 6.23

9.59



(f)  $\alpha = 15^\circ$ ,  $C_L \approx 1.01$ .

Figure 15.- Concluded.

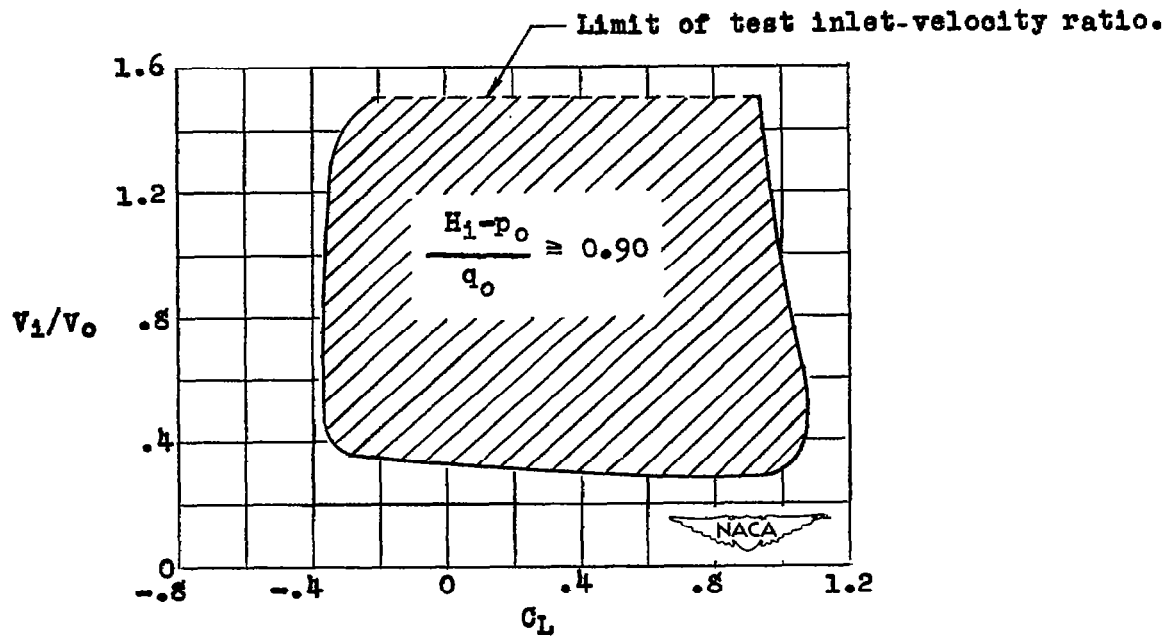
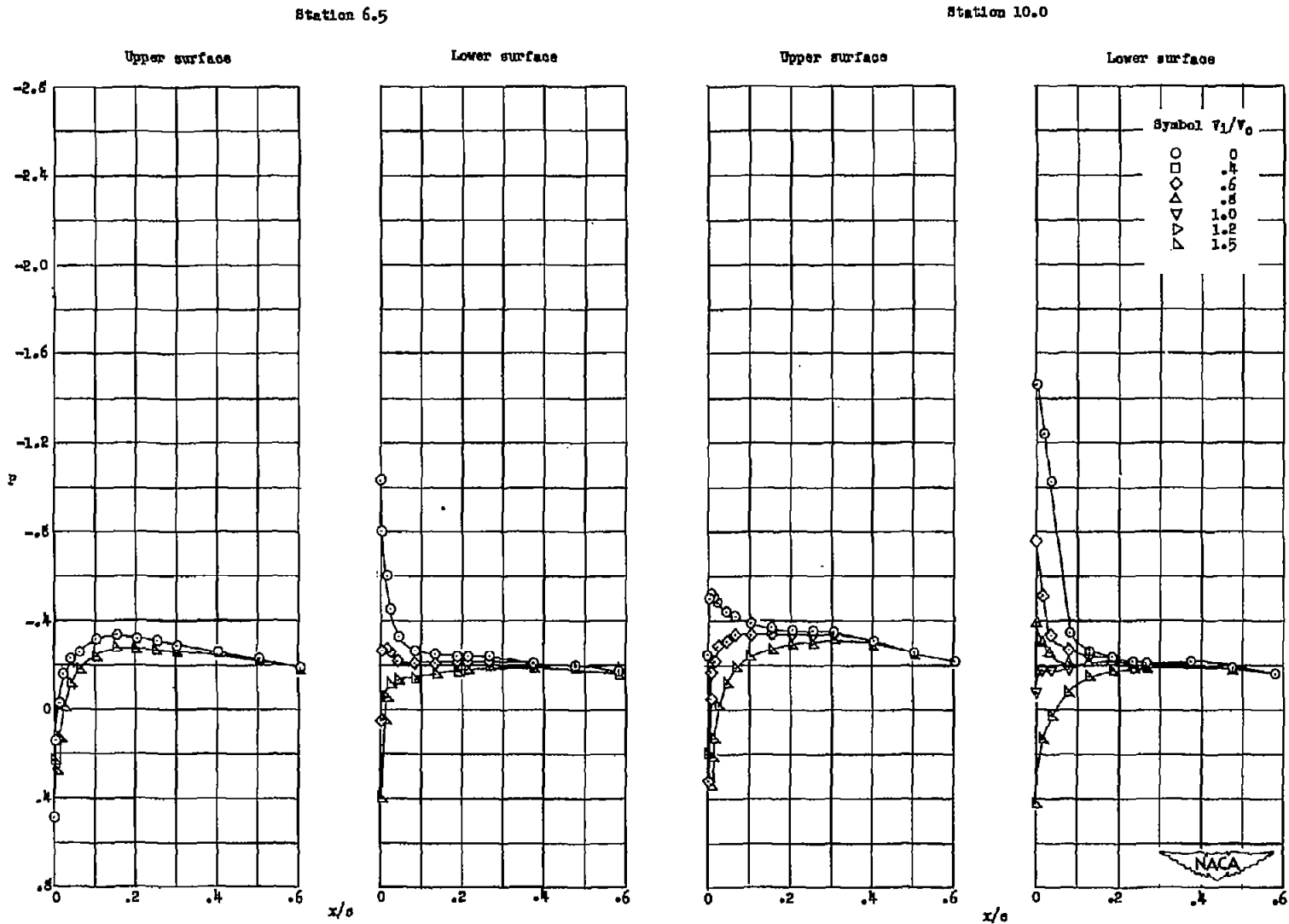
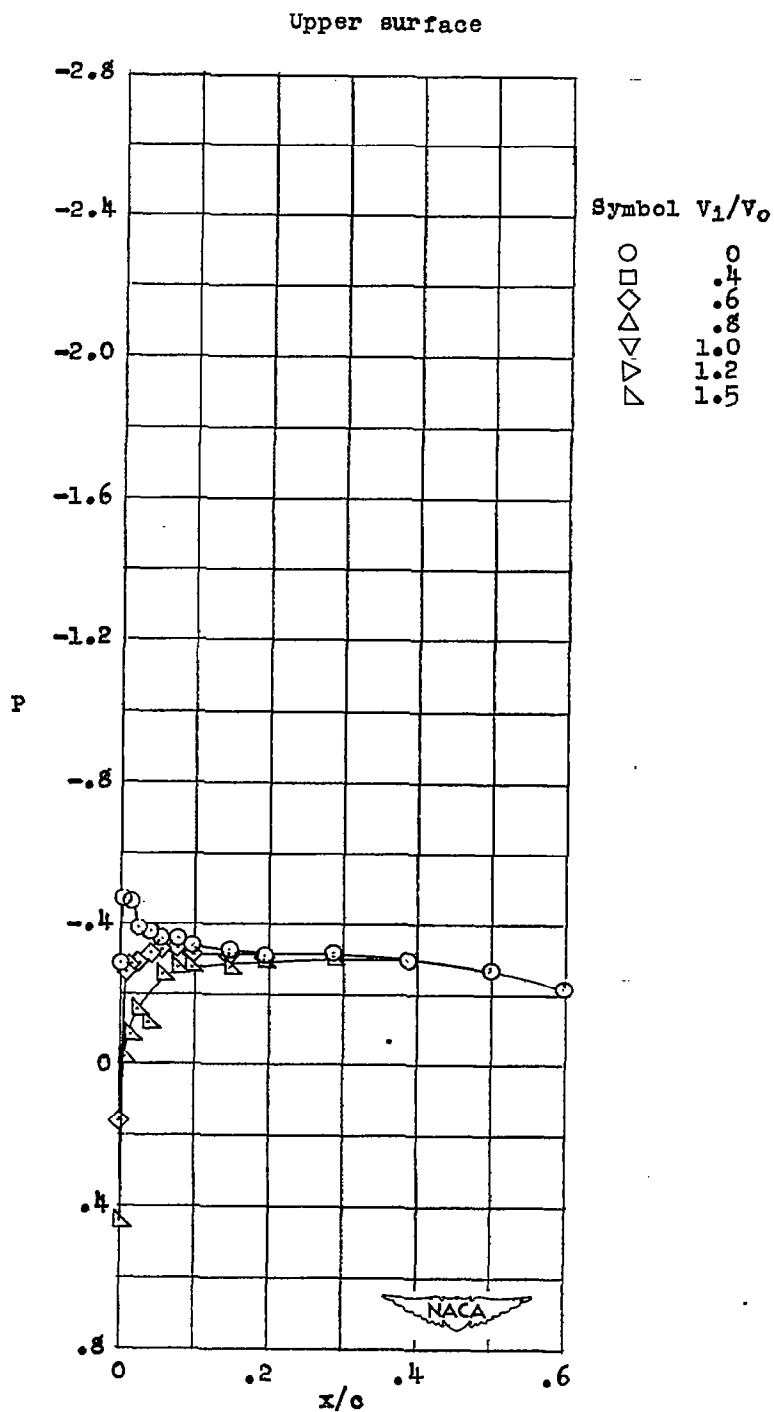


Figure 16.- Range of lift coefficient and inlet-velocity ratio for which the estimated inlet total-pressure recovery of the final inlet model is equal to or greater than  $0.90q_0$ .



(a) Station 6.5 and 10.0,  $\alpha = 0^\circ$ ,  $C_L \approx 0.06$ .

Figure 17.- Static-pressure distribution over the external surfaces of the final inlet model at the several measuring stations.

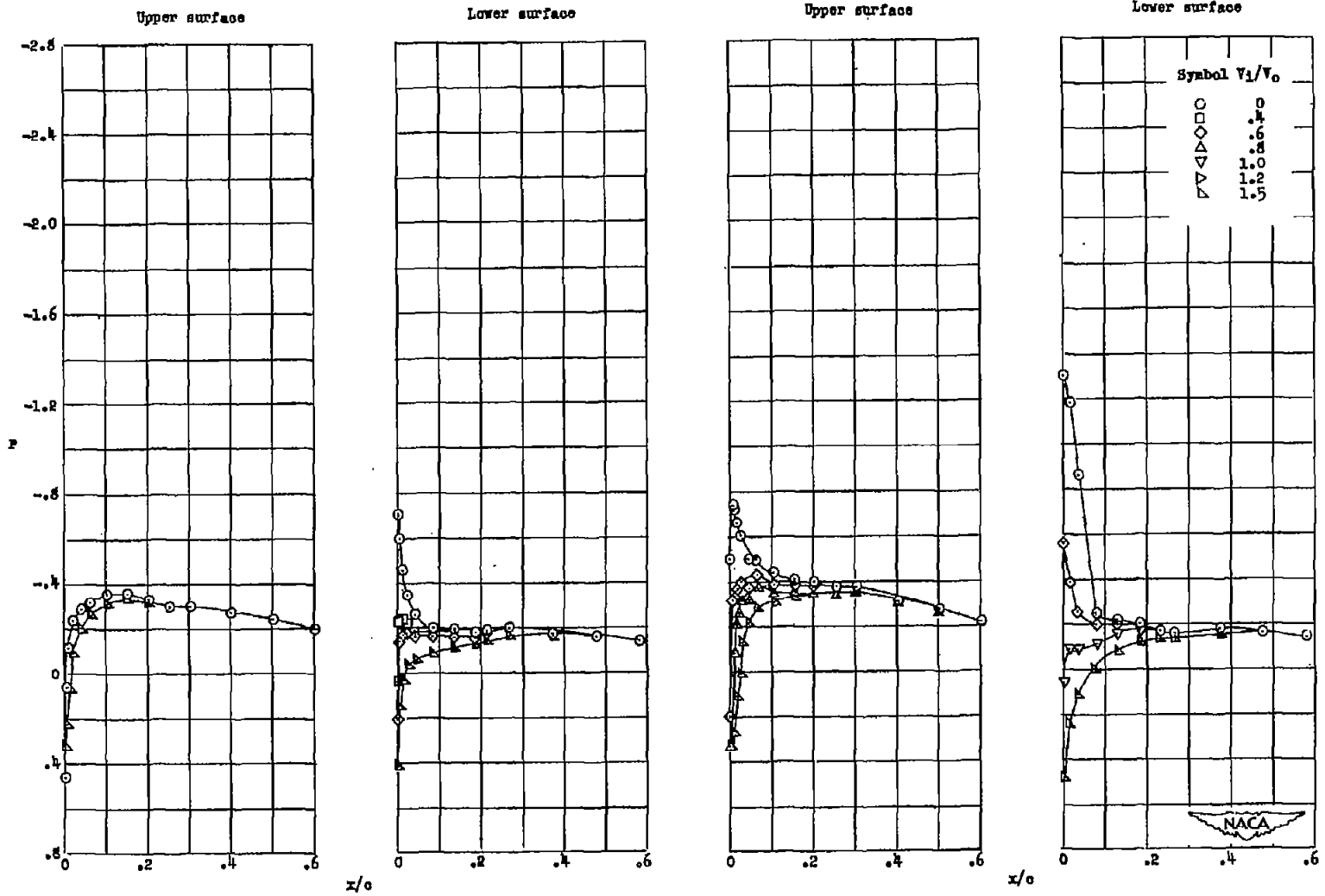


(b) Station 13.0,  $\alpha = 0^\circ$ ,  $C_L \approx 0.06$ .

Figure 17.- Continued.

Station 6.5

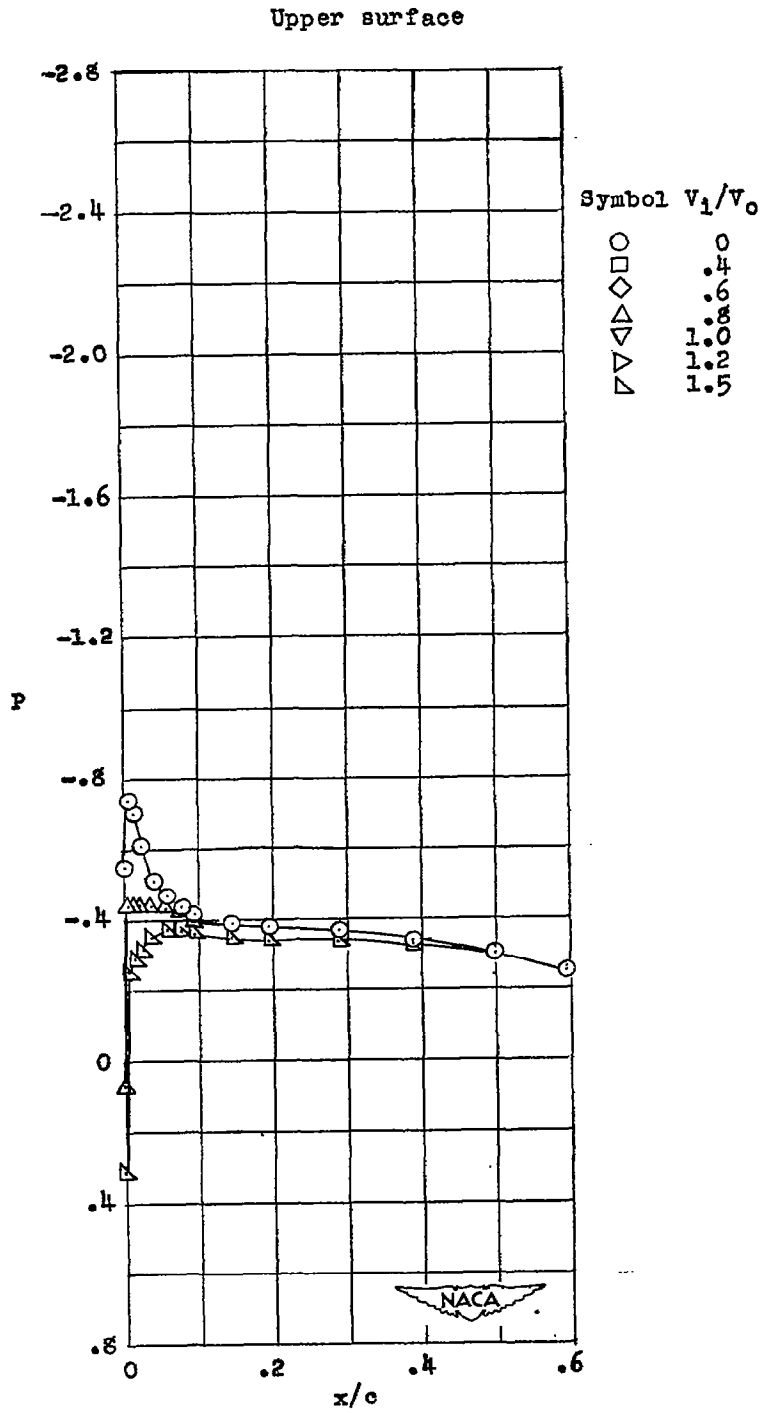
Station 10.0



(c) Station 6.5 and 10.0,  $\alpha = 1^\circ$ ,  $C_L \approx 0.14$ .

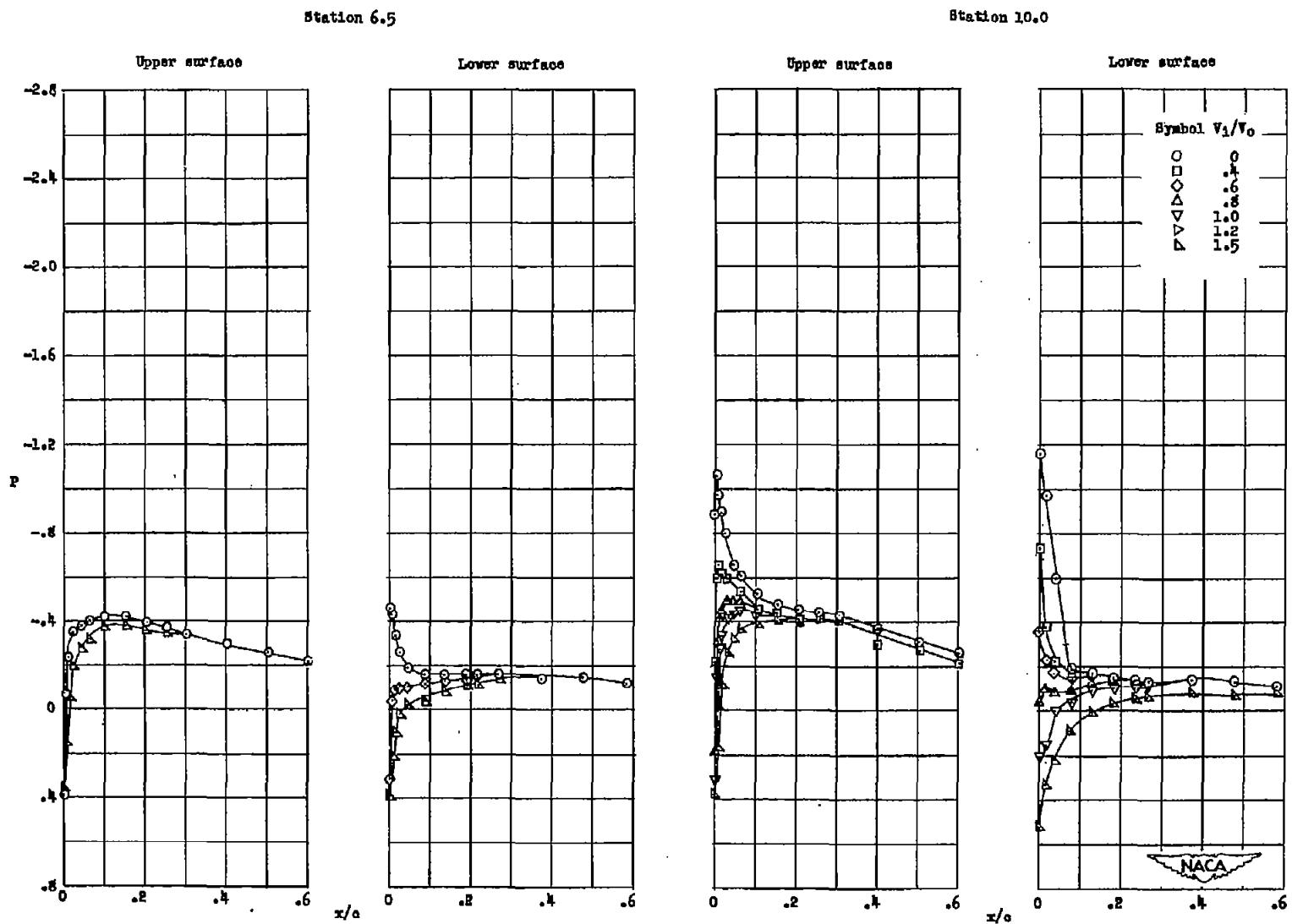
Figure 17.- Continued.





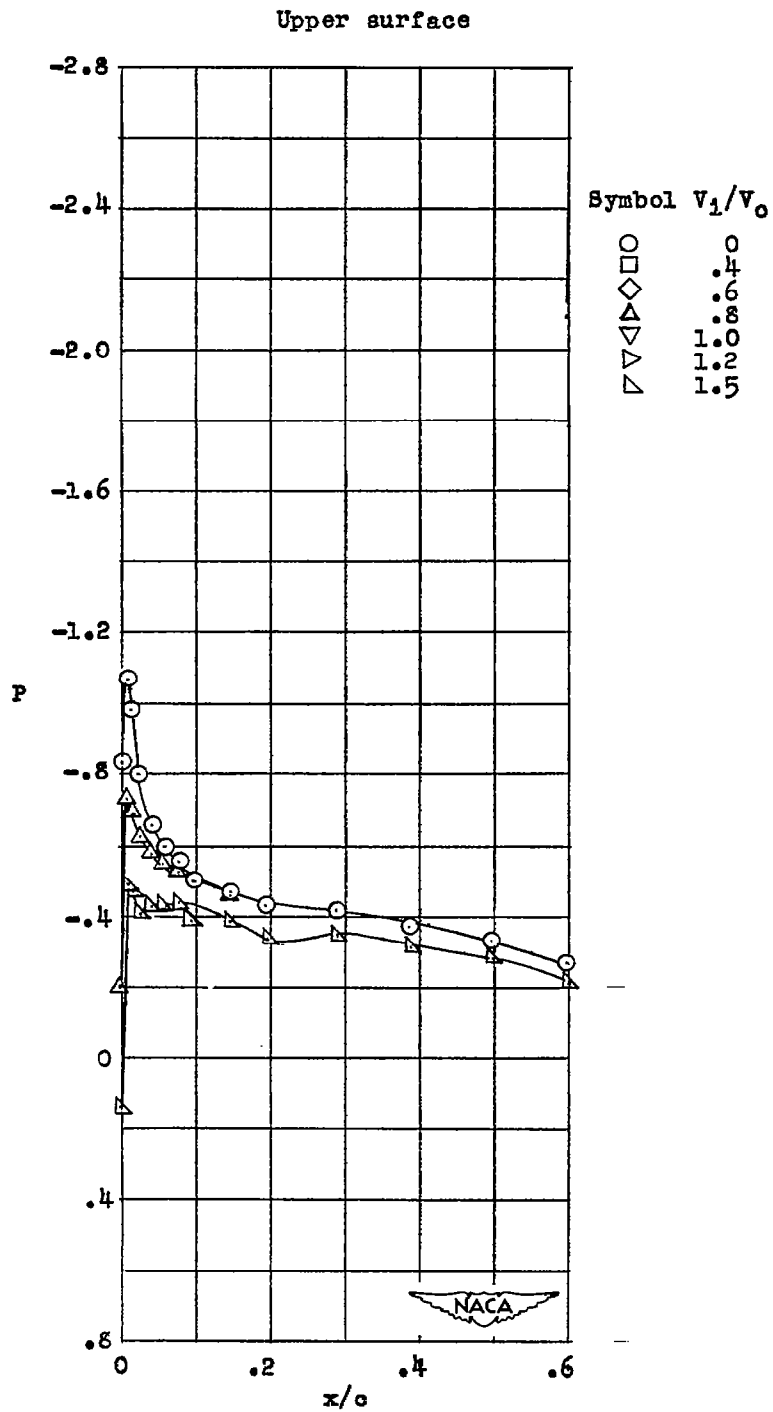
(d) Station 13.0,  $\alpha = 1^\circ$ ,  $C_L \approx 0.14$ .

Figure 17.- Continued.



(e) Station 6.5 and 10.0,  $\alpha = 2^\circ$ ,  $C_L \approx 0.23$ .

Figure 17.- Continued.

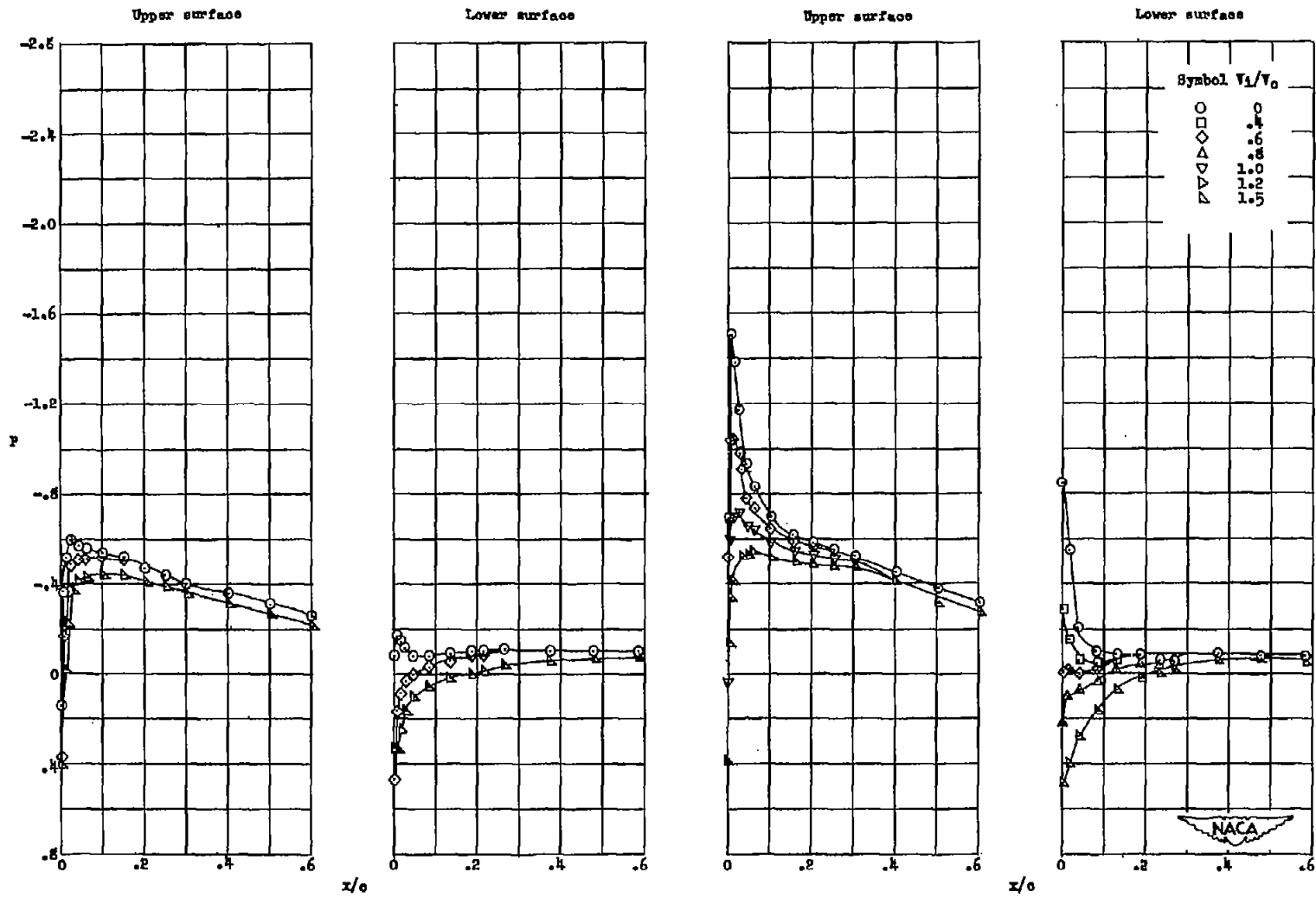


(f) Station 13.0,  $\alpha = 2^\circ$ ,  $C_L \approx 0.23$ .

Figure 17.- Continued.

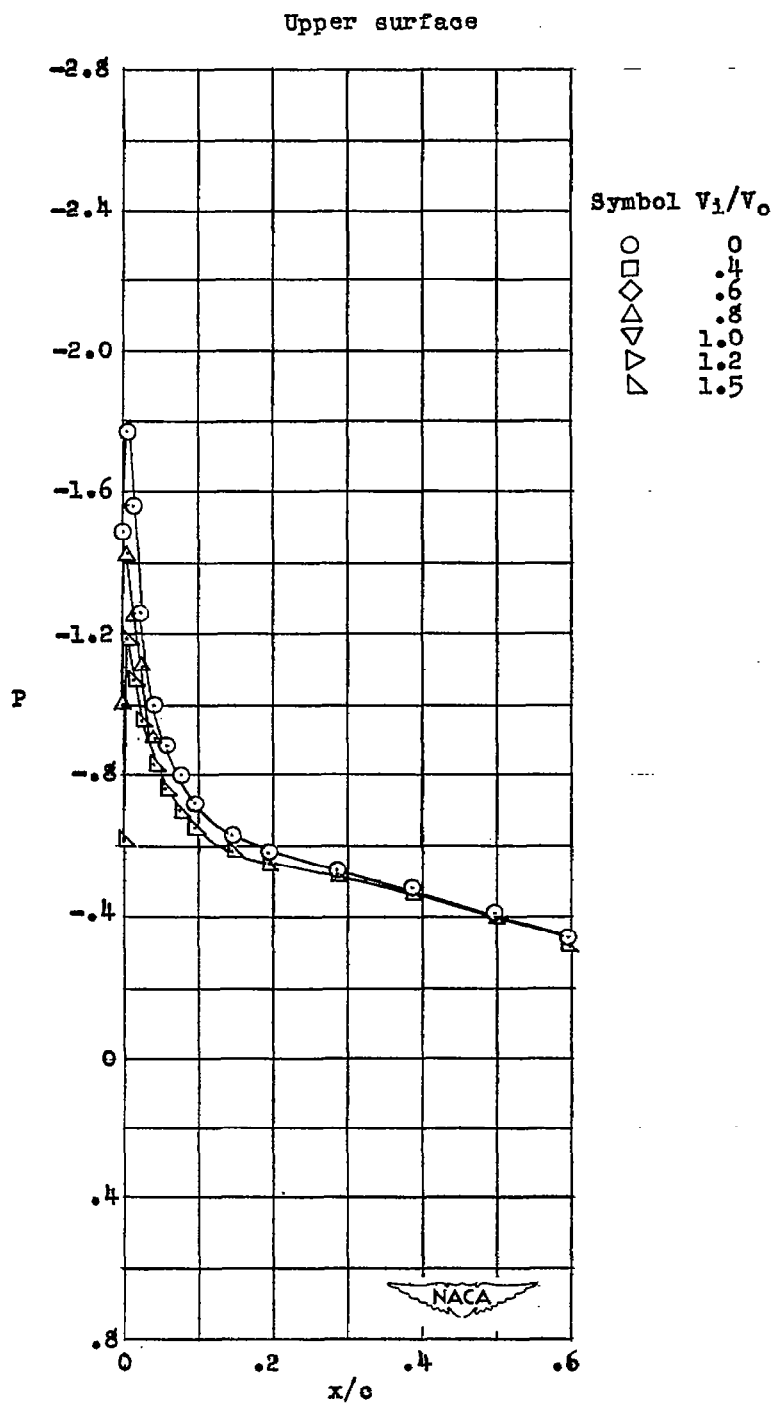
Station 6.5

Station 10.0



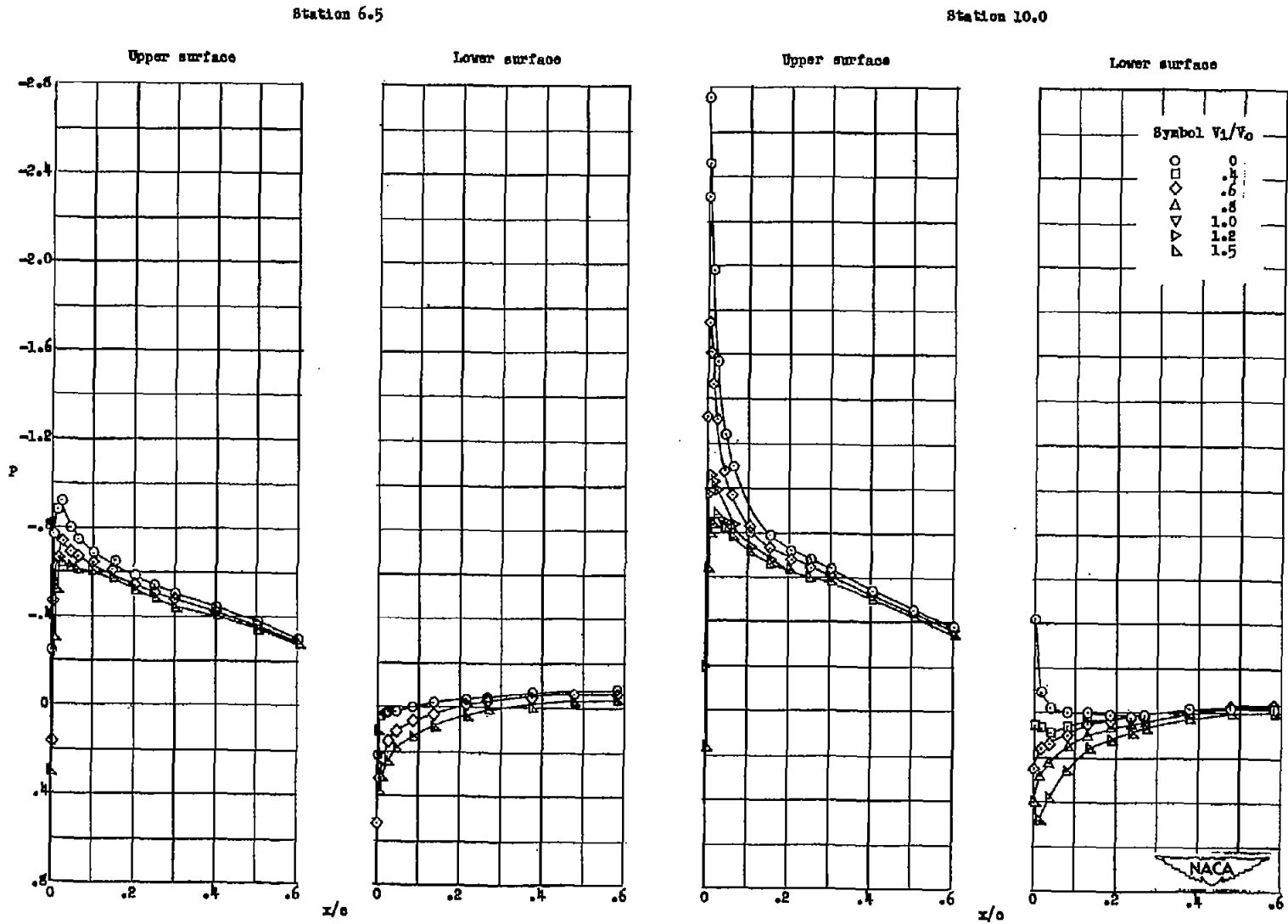
(g) Station 6.5 and 10.0,  $\alpha = 4^\circ$ ,  $C_L \approx 0.40$ .

Figure 17.- Continued.



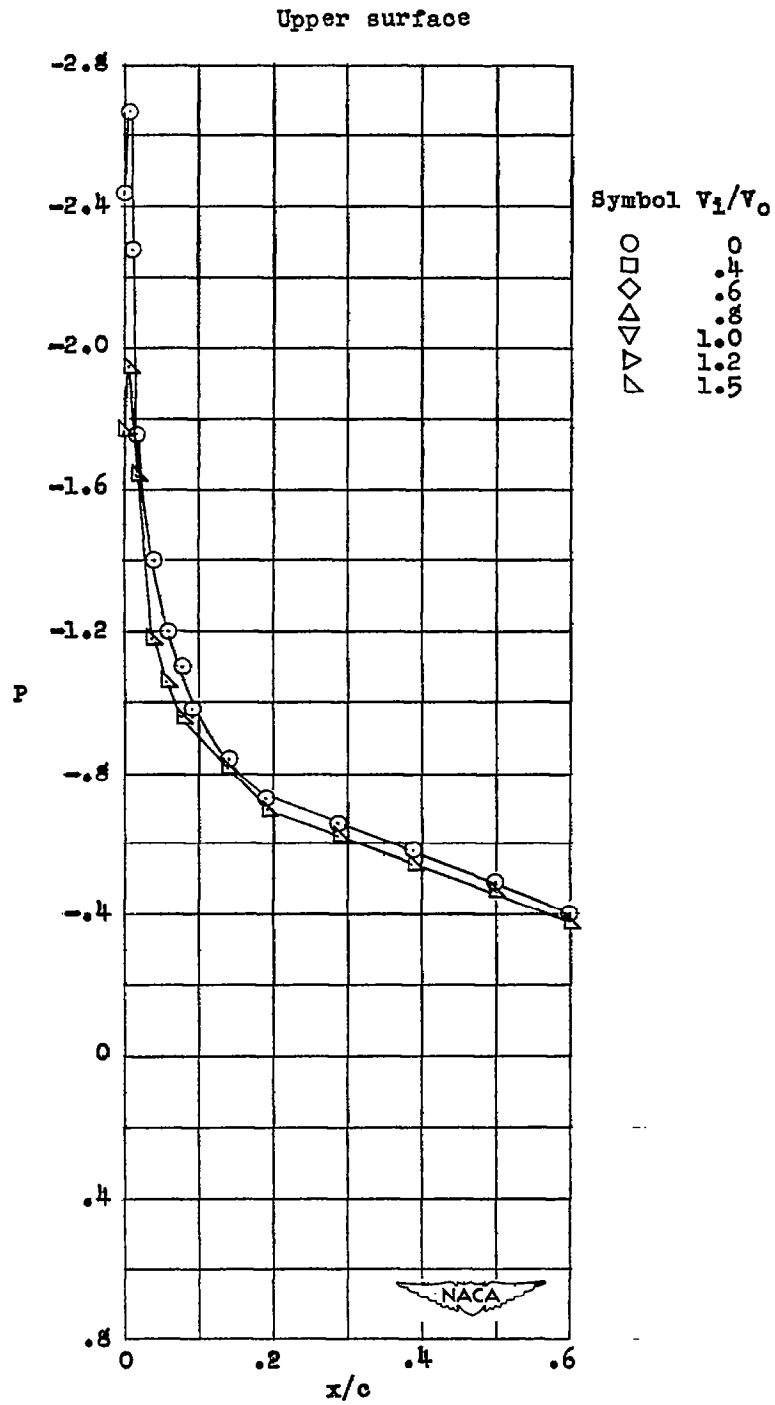
(h) Station 13.0,  $\alpha = 4^\circ$ ,  $C_L \approx 0.40$ .

Figure 17.- Continued.



(i) Station 6.5 and 10.0,  $\alpha = 6^\circ$ ,  $C_L \approx 0.58$ .

Figure 17.- Continued.



(j) Station 13.0,  $\alpha = 6^\circ$ ,  $C_L \approx 0.58$ .

Figure 17.- Concluded.

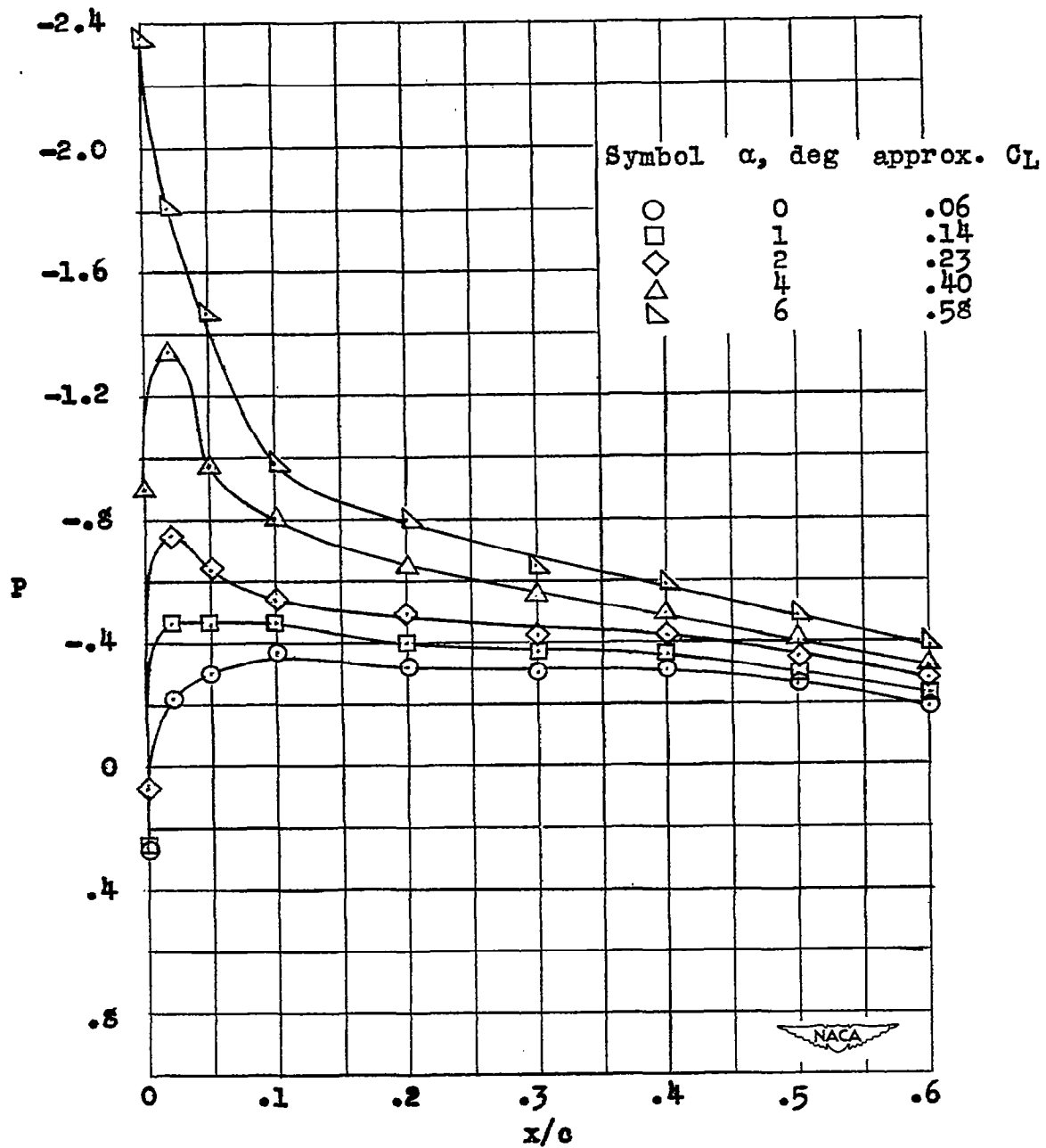


Figure 18.- Static-pressure distribution over upper-wing surface at midspan station 18 of final inlet (NACA 64-008 section streamwise).



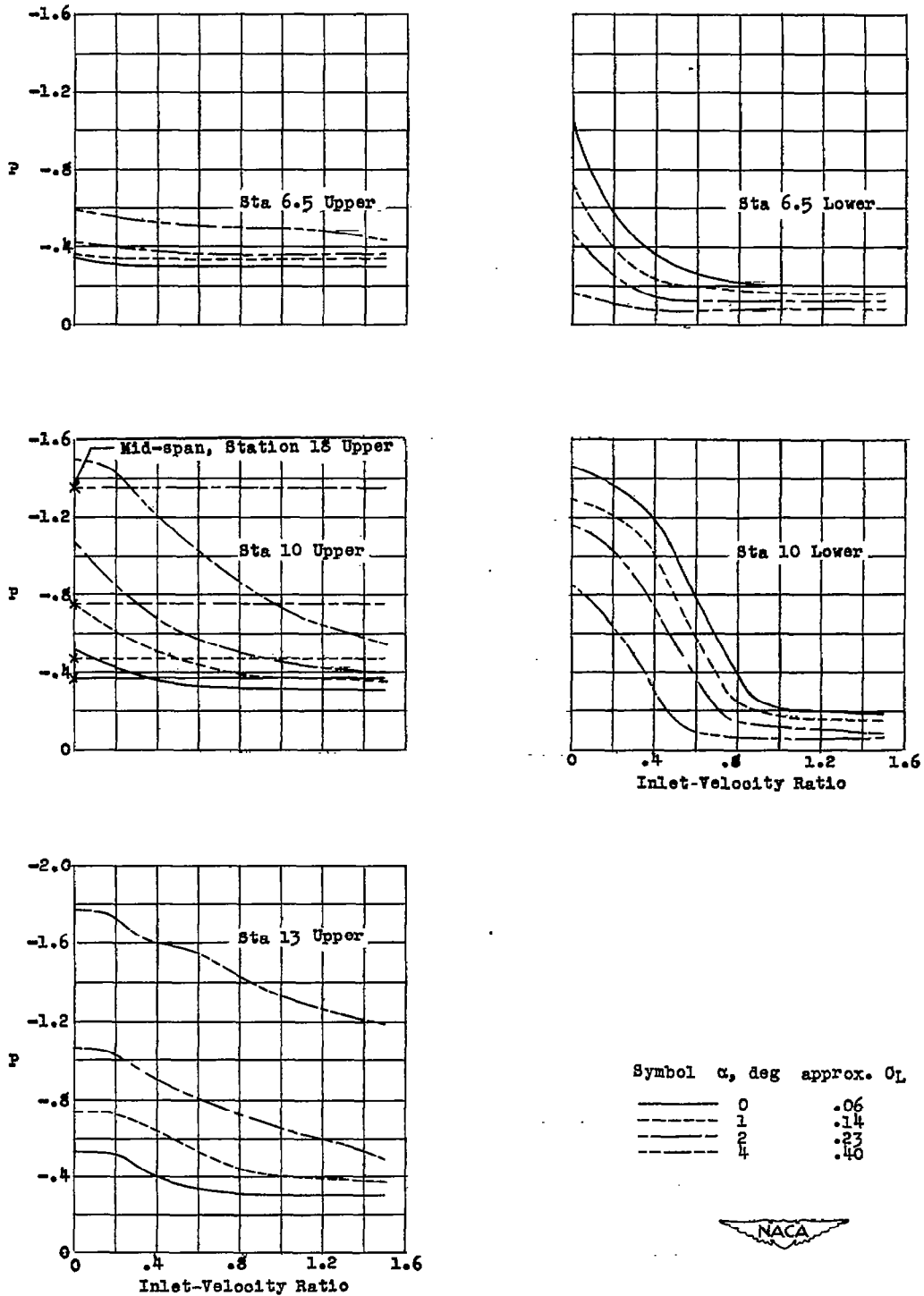


Figure 19.- Minimum external surface-pressure coefficients of the final inlet model of the several measuring stations.

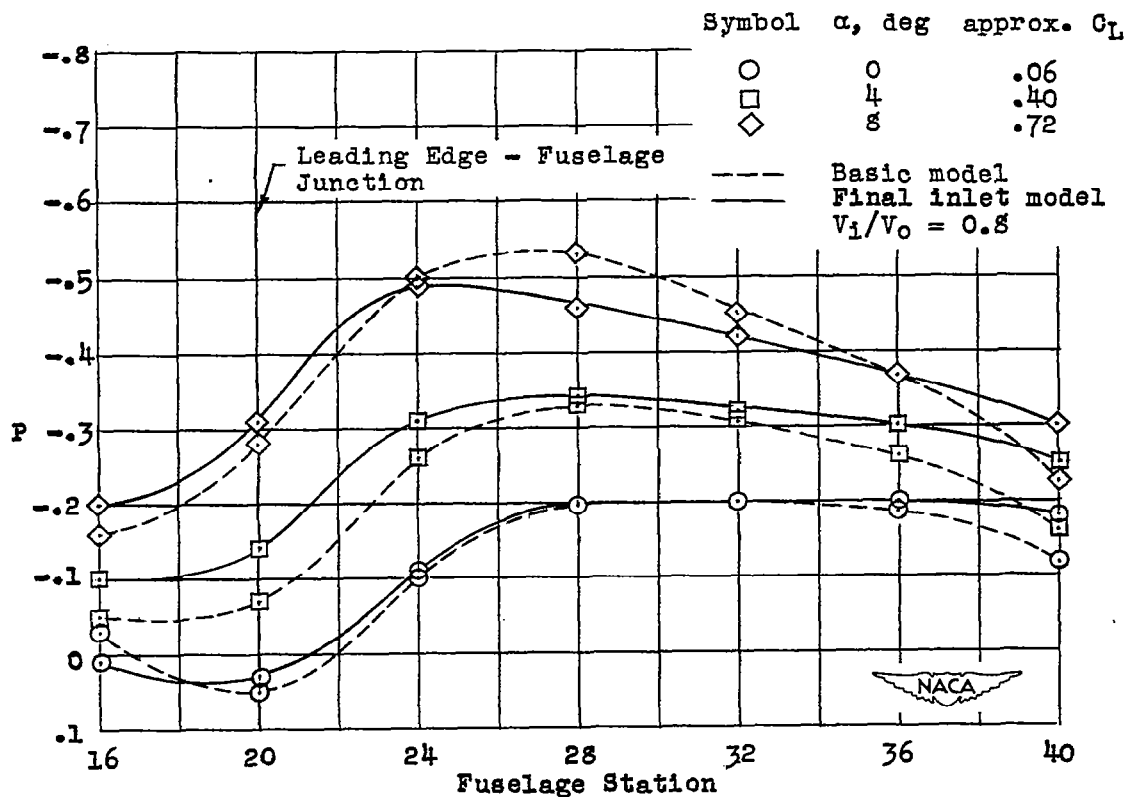
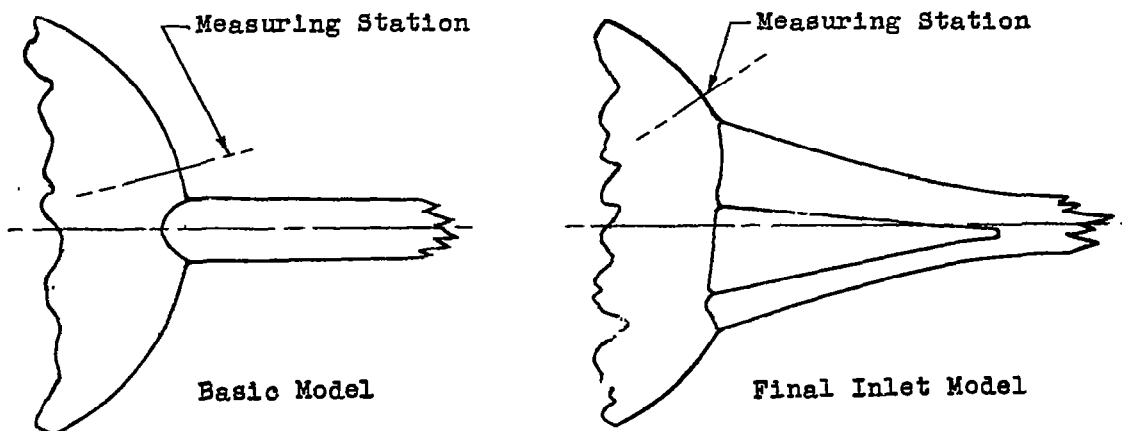


Figure 20.- Effect of increase in wing-root thickness on the fuselage pressure distribution at the wing-fuselage juncture of the final inlet model.